On the application of WKB theory for the simulation of the weakly nonlinear dynamics of gravity waves

J. Muraschko[a], M. D. Fruman[a], U. Achatz[a]*, S. Hickel[b], and Y. Toledo[c]

[a] *Institut für Atmosphäre und Umwelt, Goethe-Universität Frankfurt, Frankfurt am Main, Germany*
[b] *Institut für Aerodynamik und Strömungsmechanik, Technische Universität München, Garching by Munich, Germany*
[c] *School of Mechanical Engineering, Tel-Aviv University, Tel Aviv, Israel*
*Correspondence to: Institut für Atmosphäre und Umwelt, Goethe-Universität Frankfurt, Altenhöferallee 1, D-60438 Frankfurt am Main, Germany. E-mail: achatz@iau.uni-frankfurt.de

The dynamics of internal gravity waves is modelled using WKB theory in position-wavenumber phase space. A transport equation for the phase-space wave-action density is derived for describing one-dimensional wave fields in a background with height-dependent stratification and height- and time-dependent horizontal-mean horizontal wind, where the mean wind is coupled to the waves through the divergence of the mean vertical flux of horizontal momentum associated with the waves. The phase-space approach bypasses the caustics problem that occurs in WKB ray-tracing models when the wavenumber becomes a multivalued function of position, such as in the case of a wave packet encountering a reflecting jet or in the presence of a time-dependent background flow. Two numerical models were developed to solve the coupled equations for the wave-action density and horizontal mean wind: an Eulerian model using a finite-volume method, and a Lagrangian "phase-space ray tracer" that transports wave-action density along phase-space paths determined by the classical WKB ray equations for position and wavenumber. The models are used to simulate the upward propagation of a Gaussian wave packet through a variable stratification, a wind jet, and the mean flow induced by the waves. Results from the WKB models are in good agreement with simulations using a weakly nonlinear wave-resolving model as well as with a fully nonlinear large-eddy-simulation model. The work is a step toward more realistic parameterizations of atmospheric gravity waves in weather and climate models. **Copyright © 2013 Royal Meteorological Society**

Key Words: gravity waves; WKB theory

Received . . .

Citation: . . .

1. Introduction

It is well established that gravity waves play an important role in the dynamics of the atmosphere. Excited in the troposphere through processes such as flow over topography, convection, and jet imbalance, they transport momentum and energy into the stratosphere and mesosphere, where they break and deposit their momentum. This forcing – known as gravity-wave drag – helps maintain the large-scale circulation in the middle atmosphere. In climate models and models used for weather forecasting, gravity-wave drag must be parameterized, since the models cannot resolve the entire range of gravity-wave scales, much less the even smaller scales involved in gravity wave breaking and wave-turbulence interactions. For an overview of atmospheric gravity waves and the parameterization

of gravity-wave drag in weather and climate models see Fritts and Alexander (2003), Kim *et al.* (2003) and Alexander *et al.* (2010).

Many parameterization schemes (Lindzen 1981; Alexander and Dunkerton 1999; Warner and McIntyre 2001; Song and Chun 2008) are based on Wentzel-Kramer-Brillouin (WKB) theory (Bretherton 1966; Grimshaw 1975; Müller 1976), where the amplitude, wavelength and frequency of the waves are represented as functions of space and time that vary slowly compared to the scales of the waves themselves. WKB theory leads to the *ray equations*, which describe the propagation and evolution of wave properties along paths everywhere parallel to the local group velocity. Numerical models based on the ray equations, colloquially known as *ray tracers*, have been used for the interpretation of gravity wave observations (e.g. Eckermann 1992; Marks and Eckermann 1995; Hertzog *et al.* 2002) and for studying the evolution of gravity wave fields in realistic large-scale flows. Examples of the latter include the three-dimensional ray tracer developed by Song and Chun (2008) to simulate gravity-wave drag induced by cumulus convection and the ray tracer used by Senf and Achatz (2011) for studying the impact of thermal tides on the propagation and dissipation of gravity waves.

Gravity-wave-drag parameterizations based on WKB theory (such as that of Warner and McIntyre 2001) neglect the effect of transience in the large-scale flow on the waves. Given a (discrete or continuous) spectrum of emitted waves and an instantaneous background state, these schemes use steady-state WKB theory to calculate the wave properties at all heights and the mean flow is modified accordingly based on parameterization-specific rules related to, for example, static instability and critical levels. However, the steady-state assumption is probably not justified when there are significant interactions between gravity waves and solar tides (Senf and Achatz 2011) or between small-scale parameterized waves and large-scale explicitly resolved waves (discussed in several studies on internal waves in the upper ocean interacting with inertial waves, see Vanderhoff *et al.* 2008, 2010, and references therein). Indeed, current general circulation models have horizontal resolutions of tens of kilometres and therefore resolve a large part of the gravity-wave spectrum (e.g. Watanabe *et al.* 2008). It is likely that in such cases the time scale of the background variations is not long compared to that of the evolution of the wave packet (not to be confused with the period of the waves themselves). The steady state approximation is also not consistent with localized wave packets excited by a transient source, such as a convective event, which induce a time-dependent mean flow.

As will be shown, when transience in the background is accounted for, solutions to the ray equations tend to become multivalued functions of space. This is an example of the *caustics* problem (Lighthill 1978), where two or more rays intersect and the ray equation for wave-action density (the quantity representing wave amplitude in WKB theory) becomes ill-defined. The formalism used by Hertzog *et al.* (2002) (following Dewar 1970; Dubrulle and Nazarenko 1997) avoids the caustics problem by casting the WKB equations in the form of a transport equation for the wave-action density in position-wavenumber phase space. The same formalism was also used by Bühler and McIntyre (1999) to study propagation of Kelvin-Helmoltz shear-generated gravity waves through the summer stratosphere.

A particular way in which the background becomes time dependent is through the forcing due to the divergence of the momentum flux associated with the waves themselves. Sutherland (2001) showed that the propagation of a horizontally periodic, vertically compact wave packet is strongly modified by the interaction between the waves and the wave-induced mean flow, a phenomenon known as *self acceleration*, and that a weakly nonlinear* system coupling the wave packet to the induced mean flow – but neglecting other wave-wave interactions – is sufficient to capture most of the nonlinear dynamics (note that unlike, for example, the effect of breaking waves or waves encountering a critical level, this kind of mean flow forcing is reversible). The gravity-wave momentum flux in a WKB model is a function of position, wavenumber and wave action density so it can be readily coupled to an equation for the mean flow to yield a weakly nonlinear WKB model.

The same approach for overcoming the caustics problem is already in common use in the field of surface gravity waves in the ocean. There, the wave-action-density equation is solved for forecasting and engineering purposes in either a position-wavenumber or a position-frequency-direction formulation. Both are employed operationally by various wave models (see, e.g., Booij *et al.* 1999; WAMDI Group 1988; Benoit *et al.* 1996; Tolman 1991) and are coupled in the same weakly nonlinear manner with ocean circulation models (see Dietrich *et al.* 2011; Roland *et al.* 2009, 2012).

The aim of the present study is to use WKB theory to describe the propagation of a gravity wave packet in a time-dependent background flow while accounting for the effect of the waves on the background flow. We show that the phase-space WKB approach is able to describe the weakly nonlinear coupled system while avoiding the caustics problem. For simplicity, the Boussinesq approximation is used, and the study is restricted to horizontally uniform, vertically localized gravity wave packets. Simple test cases are presented to illustrate the effects of the wave field on the mean flow and of the wave-induced mean flow on the wave field.

Two numerical algorithms are proposed for solving the phase-space WKB equations coupled to an equation for the evolution of the mean flow. The first uses a finite-volume method to solve the transport equation for wave-action density in position-wavenumber phase space, and the second is a ray tracer (in phase space) that exploits the area preserving property of the phase space flow. Simulations with the WKB models are compared to simulations with two explicitly wave-resolving models – a weakly nonlinear model and a fully nonlinear large-eddy-simulation (LES) model.

The paper is structured as follows. In section 2, an explanation and derivation of the theory is given. In section 3, the ray equations are reviewed and the caustics problem that arises in, for example, cases of self-accelerated wave packets and wave packets encountering a strong wind jet is illustrated. The equations governing the weakly nonlinear evolution of gravity-wave packets using WKB theory in phase space are derived in section 4. The two numerical implementations of the weakly nonlinear phase-space WKB equations as well as the two validation models are described in section 5. Finally, section 6 presents the results of a series

*Some authors (e.g. Fritts and Dunkerton 1984) refer to this system as "quasi-linear"

of experiments, with an emphasis on test cases which lead to caustics.

2. The weakly nonlinear Boussinesq equations

The theory developed here for the weakly nonlinear evolution of internal gravity wave packets assumes that the background is a variably stratified fluid with a time- and height-dependent horizontal-mean horizontal flow. The influence of the Coriolis force is neglected, as are molecular viscosity and diffusion. The waves propagate in the xz-plane, have constant horizontal wavenumber k and time- and height-dependent vertical wavenumber and amplitude. We make the standard WKB assumption that the background fields and wave properties vary on time and space scales long compared to the period and vertical wavelength of the waves.

Except for the increase in wave amplitude with height in a stably stratified environment, the dynamics of internal gravity waves can be well described by the Boussinesq equations:

$$\frac{Du}{Dt} + \frac{\partial p}{\partial x} = 0 \,, \tag{1a}$$

$$\frac{Dw}{Dt} + \frac{\partial p}{\partial z} - b = 0 \,, \tag{1b}$$

$$\frac{Db}{Dt} + N^2 w = 0 \,, \tag{1c}$$

$$\frac{\partial u}{\partial x} + \frac{\partial w}{\partial z} = 0 \,, \tag{1d}$$

where u and w are the horizontal and vertical components of velocity, p is the departure from the background hydrostatic pressure divided by a constant reference density, N is the height dependent Brunt-Väisälä frequency, b is the buoyancy, and g is the constant acceleration due to gravity. For application to the atmosphere, N and b are defined in terms of potential temperature $\theta = \theta_0 + \overline{\theta}(z) + \theta'(x,z,t)$, where θ_0 is a constant and $\overline{\theta}(z)$ a fixed profile, via $N^2 = (g/\theta_0)\mathrm{d}\overline{\theta}/\mathrm{d}z$ and $b = g\theta'/\theta_0$. The two-dimensional material derivative is

$$\frac{D}{Dt} = \frac{\partial}{\partial t} + u\frac{\partial}{\partial x} + w\frac{\partial}{\partial z} \,. \tag{2}$$

To derive the equations governing the weakly nonlinear dynamics of the waves, we begin by linearizing (1) about a time- and height-dependent horizontal flow $U(z,t)$. Next we derive the WKB ray equations governing the evolution of gravity waves in the linearized system. Finally we let $U(z,t)$ evolve in time depending on the divergence of the vertical flux of horizontal momentum associated with the waves.

The linearized equations may be written

$$\frac{\partial u'}{\partial t} + U\frac{\partial u'}{\partial x} + w'\frac{\partial U}{\partial z} + \frac{\partial p'}{\partial x} = 0 \,, \tag{3a}$$

$$\frac{\partial w'}{\partial t} + U\frac{\partial w'}{\partial x} + \frac{\partial p'}{\partial z} - b' = 0 \,, \tag{3b}$$

$$\frac{\partial b'}{\partial t} + U\frac{\partial b'}{\partial x} + N^2 w' = 0 \,, \tag{3c}$$

$$\frac{\partial u'}{\partial x} + \frac{\partial w'}{\partial z} = 0 \,, \tag{3d}$$

where $u' = u - U$, $w' = w$, $p' = p$ and $b' = b$.

We assume a solution to (3) in the form of a single gravity-wave packet with period and wavelength small compared to the scales of the background and follow the development in Achatz *et al.* (2010) by postulating the ansatz

$$\begin{pmatrix} u'(x,z,t) \\ w'(x,z,t) \\ b'(x,z,t) \\ p'(x,z,t) \end{pmatrix} = \sum_{j=0}^{\infty} \epsilon^j \, \Re \left\{ \begin{pmatrix} \hat{u}_j(Z,T) \\ \hat{w}_j(Z,T) \\ \hat{b}_j(Z,T) \\ \hat{p}_j(Z,T) \end{pmatrix} \exp\left[ikx + \frac{i\Theta(Z,T)}{\epsilon} \right] \right\} \,, \tag{4}$$

where ϵ is a small parameter, $\hat{u}_j$, $\hat{w}_j$, $\hat{b}_j$ and $\hat{p}_j$ are single-valued time- and height-dependent complex wave amplitudes, $Z = \epsilon z$ and $T = \epsilon t$ are "slow" height and time coordinates, k is the constant horizontal wavenumber, and $\Theta(Z,T)/\epsilon$ is the fast-varying time- and height-dependent part of the wave phase. Following Hayes (1970), we define

$$m(Z,T) = \frac{\partial \Theta}{\partial Z} \,, \quad \omega(Z,T) = -\frac{\partial \Theta}{\partial T} \,, \tag{5}$$

the time- and height-dependent vertical wavenumber and frequency.

Inserting (4) into (3) and collecting terms in powers of ϵ yields

$$\begin{pmatrix} -i\hat{\omega} & 0 & 0 & ik \\ 0 & -i\hat{\omega} & -N & im \\ 0 & N & -i\hat{\omega} & 0 \\ ik & im & 0 & 0 \end{pmatrix} \begin{pmatrix} \hat{u}_0 \\ \hat{w}_0 \\ \hat{b}_0/N \\ \hat{p}_0 \end{pmatrix} + \epsilon \left\{ \begin{pmatrix} -i\hat{\omega} & 0 & 0 & ik \\ 0 & -i\hat{\omega} & -N & im \\ 0 & N & -i\hat{\omega} & 0 \\ ik & im & 0 & 0 \end{pmatrix} \begin{pmatrix} \hat{u}_1 \\ \hat{w}_1 \\ \hat{b}_1/N \\ \hat{p}_1 \end{pmatrix} + \begin{pmatrix} \partial\hat{u}_0/\partial T + (\partial U/\partial Z)\hat{w}_0 \\ \partial\hat{w}_0/\partial T + \partial\hat{p}_0/\partial Z \\ (1/N)\partial\hat{b}_0/\partial T \\ \partial\hat{w}_0/\partial Z \end{pmatrix} \right\} = \mathcal{O}\left(\epsilon^2\right) \,, \tag{6}$$

where

$$\hat{\omega} \equiv \omega - kU \tag{7}$$

is the *intrinsic frequency* (i.e. the frequency observed in a reference frame moving with the mean flow). To $\mathcal{O}(1)$,

$$\mathbf{M} \begin{pmatrix} \hat{u}_0 \\ \hat{w}_0 \\ \hat{b}_0/N \\ \hat{p}_0 \end{pmatrix} = 0 \,,$$

$$\text{where} \quad \mathbf{M} \equiv \begin{pmatrix} -i\hat{\omega} & 0 & 0 & ik \\ 0 & -i\hat{\omega} & -N & im \\ 0 & N & -i\hat{\omega} & 0 \\ ik & im & 0 & 0 \end{pmatrix} \,. \tag{8}$$

For nontrivial solutions to (8), the determinant of $\mathbf{M}$ must vanish, yielding

$$\hat{\omega}^2 = (\omega - kU)^2 = \frac{N^2 k^2}{k^2 + m^2} \tag{9}$$

and

$$(\hat{u}_0, \hat{w}_0, \hat{b}_0/N, \hat{p}_0) = a\left(-i\frac{\hat{\omega}}{k}, i\frac{\hat{\omega}}{m}, \frac{N}{m}, -i\frac{\hat{\omega}^2}{k^2}\right) , \quad (10)$$

where a is a complex constant whose magnitude represents the wave amplitude in nondimensional units defined such that $|a| > 1$ implies the waves are "statically unstable". Equations (9) and (10) are the dispersion relation and polarization relations for gravity waves in a uniform background with N and U equal to their instantaneous local values. For convenience we introduce the functions

$$\Omega_\pm(m, z, t) \equiv kU(z, t) \pm \frac{kN(z)}{\sqrt{k^2 + m^2}} , \quad (11)$$

which will be used later to derive the ray equations. Note that the subscript on $\Omega_\pm$ corresponds to the sign of the intrinsic horizontal phase speed.

Multiplying the $\mathcal{O}(\epsilon)$ terms in (6) by the complex conjugate of the polarization relations vector in (10)[†], using (9) and (10) once more, and transforming back into the fast time and height variables yields the wave-action conservation law

$$\frac{\partial A}{\partial t} + \frac{\partial (c_{gz} A)}{\partial z} = 0 , \quad (12)$$

where $c_{gz} \equiv \partial\Omega_\pm/\partial m$ is the *group velocity*, and $A \equiv E/\hat{\omega}$ is the *wave-action* density, with E the wave total energy density (energy per unit mass)

$$E \equiv \frac{1}{4}\left(|\hat{u}_0|^2 + |\hat{w}_0|^2 + \frac{|\hat{b}_0|^2}{N^2}\right) = \frac{|\hat{b}_0|^2}{2N^2} . \quad (13)$$

Equation (12) governs the evolution of the wave amplitude $|a|$, which satisfies

$$|a|^2 = \frac{2m^2\hat{\omega}}{N^2} A . \quad (14)$$

The equation for the evolution of the mean flow is obtained by writing (1a) in the flux form

$$\frac{\partial u}{\partial t} + \frac{\partial \left(u^2\right)}{\partial x} + \frac{\partial (uw)}{\partial z} + \frac{\partial p}{\partial x} = 0 . \quad (15)$$

Averaging in x over one horizontal wavelength of the perturbations eliminates the x-derivatives and the linear perturbation terms and gives the momentum conservation law for a horizontally periodic wave packet with vertically varying amplitude:

$$\frac{\partial U}{\partial t} = -\frac{\partial (\overline{u'w'})}{\partial z} , \quad (16)$$

where the overbar denotes averaging over x assuming periodic boundary conditions. Equation (16) can be used to couple the mean flow to the linearized Boussinesq equations (3). Using the definition of wave-action density and the polarization relations (10) one can show that the horizontal mean of horizontal momentum flux is

$$\overline{u'w'} = Akc_{gz} , \quad (17)$$

and, with (12), that

$$\frac{\partial}{\partial t}(U - kA) = 0 , \quad (18)$$

which expresses the connection between the mean momentum and the wave *pseudomomentum* $P = kA$ (shown by Acheson 1976). Notice that for gravity waves in a shear flow, wave action is conserved, as opposed to wave energy which is exchanged with the mean flow. It can be shown using Hamiltonian methods (Scinocca and Shepherd 1992; Bühler 2009) that pseudomomentum, defined as the conserved perturbation quantity associated with symmetry of the Hamiltonian and the mean flow with respect to translation in space, can be written (in the small amplitude limit) as

$$P = \overline{\frac{b'}{N^2}\left(\frac{\partial u'}{\partial z} - \frac{\partial w'}{\partial x}\right)} , \quad (19)$$

and, using (4), (9) and (10) that, to $\mathcal{O}(\epsilon)$, (19) is equivalent to $P = kA$. Since, from (10), b' and w' are out of phase by $\pi/2$, the horizontal-mean vertical flux of buoyancy $\overline{b'w'}$ vanishes, so unlike the horizontal mean horizontal momentum, the horizontal mean buoyancy (and hence the stratification N^2) does not change with time due to the passage of the wave packet. From the horizontal mean of (1c), it follows that the horizontal-mean vertical wind must also vanish (as discussed by Achatz *et al.* 2010).

3. Ray tracing and caustics in physical space

Prognostic relations for the local frequency and wavenumber may be derived from (5) and (11) (Bretherton and Garrett 1968; Hayes 1970). Together with the wave-action conservation law (12), these are the *ray equations*

$$\frac{\mathrm{d}_g z}{\mathrm{d}t} = \frac{\partial \Omega_\pm}{\partial m} = \mp\frac{Nkm}{(k^2 + m^2)^{\frac{3}{2}}} \equiv c_{gz} , \quad (20a)$$

$$\frac{\mathrm{d}_g m}{\mathrm{d}t} = -\frac{\partial \Omega_\pm}{\partial z} = \mp\frac{k}{\sqrt{k^2 + m^2}}\frac{\mathrm{d}N}{\mathrm{d}z} - k\frac{\partial U}{\partial z} \equiv \dot{m} , \quad (20b)$$

$$\frac{\mathrm{d}_g \omega}{\mathrm{d}t} = \frac{\partial \Omega_\pm}{\partial t} = k\frac{\partial U}{\partial t} , \quad (20c)$$

$$\frac{\mathrm{d}_g A}{\mathrm{d}t} = -A\frac{\partial c_{gz}}{\partial z} , \quad (20d)$$

where

$$\dot{f} \equiv \frac{\mathrm{d}_g f}{\mathrm{d}t} \equiv \frac{\partial f}{\partial t} + c_{gz}\frac{\partial f}{\partial z} \quad (21)$$

is the time derivative of the quantity f in a frame moving with the local group velocity. The system (20) thus describes the variations in wave properties along paths, known as *rays*, parallel to the local group velocity.

Variations in U and N lead to changes in m and ω. Equation (20d) and any two of (20a)-(20c), with the third constrained by (9), may be solved as an initial value problem for the properties of the wave field at a point moving along a ray. A model that solves these equations for a collection of points representing an entire wave field

[†]Since $\mathbf{M}$ is anti-Hermitian, the conjugate-transpose of a vector in its (right) nullspace is in its *left nullspace*. See Achatz *et al.* (2010) for details.

is called a *ray tracer*. A challenge in developing a ray tracer is to calculate the derivative of c_{gz} on the right hand side of (20d) from information on the discrete and irregularly distributed set of ray points.

The ray equations are a powerful tool for the description of gravity-wave packets but they are limited by the WKB assumption that at each location there is exactly one local phase and amplitude. If a solution evolves in such a way that multiple ray points are at the same position, but have different values of (m, ω, A) and hence c_{gz}, then the derivative on the right hand side of (20d) will be undefined. Such a situation is an indication of a *caustic*, a set of points at which multiple rays intersect (see, e.g., Lighthill 1978).

Unfortunately, the formation of a caustic is not the exception but the rule for gravity waves propagating through realistic background flows. In the remainder of this section, we present examples of caustics arising under different circumstances. In each case, equations (20a) and (20b), together with the ray equation for horizontal position

$$\frac{\mathrm{d}_g x}{\mathrm{d}t} = U \pm \frac{Nm^2}{(k^2+m^2)^{\frac{3}{2}}} \equiv c_{gx} \tag{22}$$

(obtained by differentiating (11) with respect to k with z, m and t constant), are solved numerically for a collection of ray points initially located at $x = 0$, uniformly distributed in z, and all having the same initial value of m. The wave-action equation and the feedback of the waves on the background are neglected. In each example, k is positive, m is initially negative and the frequency is given by $\omega = \Omega_+$. The rays initialized this way represent a wave field with initially upward group velocity. In each case, a constant Brunt-Väisälä frequency of $N = 2 \times 10^{-2}$ s^{-1} is used.

Figure 1a shows rays associated with waves with horizontal wavelength $\lambda_x = 3$ km and initial vertical wavelength $\lambda_z = 3$ km reflected by a wind jet of the form

$$U(z) = U_0 \,\mathrm{sech}\left[\frac{(z-z_1)^2}{\Sigma_U^2}\right], \tag{23}$$

with peak velocity $U_0 = -5$ m s^{-1}, half-width $\Sigma_U = 3$ km and centre at $z_1 = 70$ km. During the reflection of the wave packet, there are simultaneously ray points with both upward and downward vertical group speed at points below the reflecting level.

One might not be interested in reflected wave packets, for example in a gravity-wave-drag parameterization, so in practice the downward propagating ray points might be ignored. Nevertheless, caustics tend to form in other commonplace circumstances. Figure 1b shows rays corresponding to nearly hydrostatic waves propagating through a weak background wind (amplitude 2 ms^{-1}) that varies sinusoidally in the vertical (wavelength 50 km). The waves initially have the same wavelengths everywhere ($\lambda_x = 30$ km and $\lambda_z = 3$ km) but due to the slightly varying wind shear, parts of the wave field (represented by the lower rays at $x = 0$ in the figure) "overtake" the parts immediately above. This may be explained as follows: According to (20b), m increases (decreases) along rays where $\mathrm{d}U/\mathrm{d}z$ is negative (positive). For nearly hydrostatic waves, the magnitude of the vertical group speed, given by (20a), decreases with increasing $|m|$. Since here $m < 0$ (the waves have positive vertical group speed), the parts of the wave field initially in a background with $\mathrm{d}U/\mathrm{d}z < 0$ develop higher vertical group speed than the rest of the wave field. The occurrence of caustics due to overtaking is typical of many types of dispersive waves, as discussed by Brown (2000).

Caustics often occur when the background wind is time dependent, for example in the problem discussed by Broutman and Young (1986) of high-frequency gravity waves in the upper ocean propagating through a large-scale inertial wave. An example of time-dependence leading to caustics is shown in figure 1c, in which a Gaussian wave packet with $\lambda_x = 2$ km and $\lambda_z = 2.9$ km propagates through its own "induced mean flow" – the mean wind equal to the waves' pseudomomentum (see equation 19). In the weakly nonlinear limit, such a background wind propagates upward together with the wave packet. The mean wind at various times is indicated by the thick grey lines in the figure. This is a test case taken from Sutherland (2006b) illustrating the phenomenon of *modulational instability*. When $|m| < k/\sqrt{2}$, group velocity *increases* with increasing $|m|$. As such, the lower flank of the wave packet is accelerated by positive background wind shear while the upper flank is decelerated by negative background wind shear, and again caustics occur due to overtaking. The data for the background mean wind were taken from weakly nonlinear wave-resolving simulations described in section 6.5.

A phenomenon related to caustics is that of a *critical level*. This is a level in a a shear flow where the background wind speed equals the horizontal phase speed of the waves. As the waves approach such a level, their group speed approaches zero but their vertical wavenumber tends to infinity (unlike near a reflecting level, where m passes through zero). Critical levels may be considered "caustics at infinity". An example of waves approaching a critical level is shown in figure 1d. The only difference from the example with the reflecting level is that the jet (equation 23) is in the same direction as the horizontal phase speed of the waves and has an amplitude $U_0 = 8$ ms^{-1}. As they approach a critical level, waves overturn and break due to the large local buoyancy gradients associated with increasing $|m|$ or else they decay due to viscous forces associated with the increasing velocity shear (proportional to $|m|$). Although the wave action equation (20d) diverges at a critical level like it does approaching a caustic, this is not merely an artifact of the WKB assumptions and the ray-tracing equations. There really is a build-up of wave action near a critical level and the system does become strongly nonlinear. The effect of the waves on the mean flow at a critical level must be treated with a suitable gravity-wave-drag parameterization scheme, regardless of how the waves are modeled.

The caustics problem is discussed in some detail in the review paper by Broutman *et al.* (2004).

4. WKB in phase-space

Broutman *et al.* (2004) propose using Maslov's method to solve the caustic problem in physical space. This entails solving the ray equations (or, where possible, the exact linear equations) in wavenumber space wherever caustics form in physical space and mapping the solution back into physical space using the inverse Fourier transform. The method has been shown to work well in cases where there are no caustics in wavenumber space (where position is a multivalued function of wavenumber) such as stationary

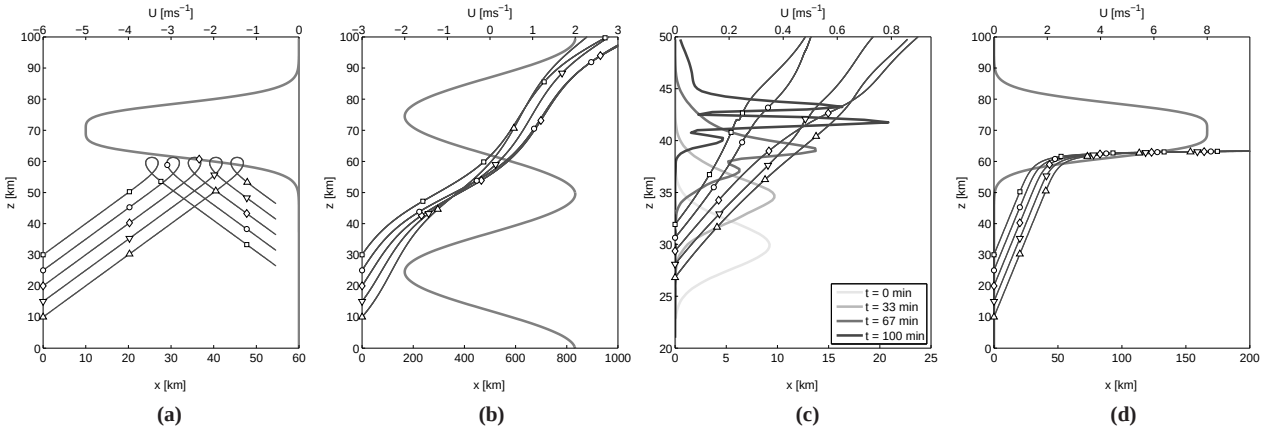

Figure 1. Examples of the caustics problem in physical space: (a) rays (thin lines) associated with waves encountering a reflecting jet (thick line); (b) waves propagating through a slowly varying alternating wind; (c) modulationally unstable waves propagating through their own induced mean flow (cf. section 6.5); (d) waves encountering a critical level due to a positive jet. Markers are placed along rays at intervals of 100 minutes in (a) and (d), 500 minutes in (b), and 33 minutes in (c).

hydrostatic mountain waves (Broutman and Rottman 2002) and trapped lee wave (Broutman *et al.* 2006) but becomes complicated when caustics occur in both physical space and wavenumber space. The same method was applied by Brown (2000) to one-dimensional surface gravity waves in a time-dependent background.

The caustics problem disappears altogether in the formalism of Hertzog *et al.* (2002), where the WKB equations are recast as a transport equation for a wave-action density in position-wavenumber phase space (hereafter simply *phase space*). This avoids the need to dynamically switch between the physical space and wavenumber space representations and is the approach adopted in the present study. The derivation presented here mainly follows Hertzog *et al.* (2002).

Consider a superposition of noninteracting WKB fields $\{m_\alpha(z,t), A_\alpha(z,t)\}$, where $\alpha \in \mathbb{R}$ is a continuous parameter, each obeying the ray equations

$$\frac{\mathrm{d}_g A_\alpha}{\mathrm{d}t} + A_\alpha \frac{\partial c_{g\alpha}(z,t)}{\partial z} = \frac{\partial A_\alpha}{\partial t} + \frac{\partial}{\partial z}\left[c_{g\alpha}(z,t) A_\alpha\right] = 0\,, \quad (24a)$$

and

$$\frac{\mathrm{d}_g m_\alpha}{\mathrm{d}t} = \frac{\partial m_\alpha}{\partial t} + c_{g\alpha}(z,t)\frac{\partial m_\alpha}{\partial z} = -\left.\frac{\partial \Omega_\pm(z,m,t)}{\partial z}\right|_{m=m_\alpha}\,, \quad (24b)$$

where $c_{g\alpha} \equiv c_{gz}(m_\alpha, z, t)$, and the phase-space wave-action density defined by

$$\mathcal{N}(z,m,t) \equiv \int_{\mathbb{R}} A_\alpha(z,t)\delta\left[m - m_\alpha(z,t)\right]\mathrm{d}\alpha\,, \quad (25)$$

where δ is the Dirac delta function. We begin by differentiating (25) with respect to time:

$$\begin{aligned}\frac{\partial \mathcal{N}}{\partial t} &= \int_{\mathbb{R}} \left[\frac{\partial A_\alpha}{\partial t}\delta(m-m_\alpha) + A_\alpha \frac{\partial}{\partial t}\delta(m-m_\alpha)\right]\mathrm{d}\alpha \\ &= \int_{\mathbb{R}} \left[\frac{\partial A_\alpha}{\partial t}\delta(m-m_\alpha) \right. \\ &\qquad \left. - A_\alpha \frac{\partial m_\alpha}{\partial t}\frac{\partial}{\partial m}\delta(m-m_\alpha)\right]\mathrm{d}\alpha\,. \quad (26)\end{aligned}$$

Using (24a), we can rewrite (26) as

$$\begin{aligned}\frac{\partial \mathcal{N}}{\partial t} = \int_{\mathbb{R}} \left[-\frac{\partial (c_{g\alpha}A_\alpha)}{\partial z}\delta(m-m_\alpha) \right. \\ \left. - A_\alpha \frac{\partial m_\alpha}{\partial t}\frac{\partial}{\partial m}\delta(m-m_\alpha)\right]\mathrm{d}\alpha\,. \quad (27)\end{aligned}$$

Rearranging terms in the integrand gives

$$\begin{aligned}\frac{\partial \mathcal{N}}{\partial t} = \int_{\mathbb{R}} \left\{-\frac{\partial}{\partial z}\left[c_{g\alpha}A_\alpha\delta(m-m_\alpha)\right] \right. \\ \left. - A_\alpha\left(c_{g\alpha}\frac{\partial m_\alpha}{\partial z} + \frac{\partial m_\alpha}{\partial t}\right)\frac{\partial}{\partial m}\delta(m-m_\alpha)\right\}\mathrm{d}\alpha\,, \quad (28)\end{aligned}$$

which, using (24b), becomes

$$\begin{aligned}\frac{\partial \mathcal{N}}{\partial t} = \int_{\mathbb{R}} \left\{-\frac{\partial}{\partial z}\left[c_{g\alpha}A_\alpha\delta(m-m_\alpha)\right] \right. \\ \left. - \frac{\mathrm{d}_g m_\alpha}{\mathrm{d}t} A_\alpha \frac{\partial}{\partial m}\delta(m-m_\alpha)\right\}\mathrm{d}\alpha\,. \quad (29)\end{aligned}$$

Since $A_\alpha(z,t)$ and $\mathrm{d}_g m_\alpha/\mathrm{d}t$ are functions only of z and t, they may be taken inside the partial m derivative:

$$\begin{aligned}\frac{\partial \mathcal{N}}{\partial t} = \int_{\mathbb{R}} \left\{-\frac{\partial}{\partial z}\left[c_{g\alpha}A_\alpha\delta(m-m_\alpha)\right] \right. \\ \left. - \frac{\partial}{\partial m}\left[\frac{\mathrm{d}_g m_\alpha}{\mathrm{d}t} A_\alpha \delta(m-m_\alpha)\right]\right\}\mathrm{d}\alpha\,, \quad (30)\end{aligned}$$

and the integral over α can be interchanged with the partial z and m derivatives to give

$$\frac{\partial \mathcal{N}}{\partial t} = -\frac{\partial}{\partial z}\int_{\mathbb{R}} c_{g\alpha} A_\alpha \delta(m-m_\alpha)\,\mathrm{d}\alpha - \frac{\partial}{\partial m}\int_{\mathbb{R}} \frac{\mathrm{d}_g m_\alpha}{\mathrm{d}t} A_\alpha \delta(m-m_\alpha)\,\mathrm{d}\alpha\,. \quad (31)$$

From the definition of the δ function, $c_{g\alpha}(z,t)$ may be replaced with $c_{gz}(m,z,t)$ in the first integral and $\mathrm{d}_g m_\alpha/\mathrm{d}t$ with $\dot{m}(m,z,t) \equiv \mathrm{d}_g m/\mathrm{d}t$ in the second, and both factors may be taken outside of the respective integrals to leave, finally,

$$\frac{\partial \mathcal{N}}{\partial t} + \frac{\partial (c_{gz}\mathcal{N})}{\partial z} + \frac{\partial (\dot{m}\mathcal{N})}{\partial m} = 0\,. \quad (32)$$

Equation (32) describes the transport of phase-space wave-action density $\mathcal{N}$ by the phase-space velocity field $(c_{gz}, \dot{m})$. From (20a) and (20b),

$$\frac{\partial c_{gz}}{\partial z} + \frac{\partial \dot{m}}{\partial m} = \frac{\partial}{\partial z}\left(\frac{\partial \Omega_\pm}{\partial m}\right) - \frac{\partial}{\partial m}\left(\frac{\partial \Omega_\pm}{\partial z}\right) = 0\,, \quad (33)$$

i.e. the phase-space velocity is divergence-free, and therefore $\mathcal{N}$ is conserved along trajectories in phase space:

$$\frac{D_r \mathcal{N}(z,m,t)}{Dt} \equiv \frac{\partial \mathcal{N}(z,m,t)}{\partial t} + c_{gz}\frac{\partial \mathcal{N}(z,m,t)}{\partial z} + \dot{m}\frac{\partial \mathcal{N}(z,m,t)}{\partial m} = 0\,. \quad (34)$$

Given an initial distribution of phase-space wave-action density $\mathcal{N}_0(z,m)$, one can calculate its distribution for any time by evolving $\mathcal{N}$ using (32) (the *Eulerian* view) or by simply advecting $\mathcal{N}_0$ conservatively along phase-space trajectories using (34) (the *Lagrangian* view).

The phase-space wave-action density may be coupled to the prognostic equation for the mean flow (16) using (17) and (25) to write

$$\overline{u'w'} = \int_{-\infty}^{\infty} k c_{gz} \mathcal{N}(m,z,t)\mathrm{d}m\,, \quad (35)$$

so that

$$\frac{\partial U}{\partial t} = -\frac{\partial}{\partial z}\int_{-\infty}^{\infty} k c_{gz} \mathcal{N}(m,z,t)\mathrm{d}m\,, \quad (36)$$

where we are implicitly assuming the induced mean flow is affected only by the self-interaction of each member of the superposition of wave fields that make up $\mathcal{N}$. Interaction between wave fields may also project on the horizontal mean, since the flux of horizontal momentum associated with one wave field, labeled α_1, due to another, labeled α_2,

$$\overline{u'_{\alpha_1} w'_{\alpha_2}} = \frac{1}{4}\left[\hat{u}_{\alpha_1}\hat{w}^*_{\alpha_2}\exp\left(\frac{\Theta_{\alpha_1}-\Theta_{\alpha_2}}{\epsilon}\right) + \hat{u}^*_{\alpha_1}\hat{w}_{\alpha_2}\exp\left(-\frac{\Theta_{\alpha_1}-\Theta_{\alpha_2}}{\epsilon}\right)\right]\,, \quad (37)$$

where Θ_α/ϵ is the fast-varying time- and height-dependent part of the phase of wave packet α (compare with the notation in the WKB ansatz (4)) is not in general zero. This effect is not captured by the WKB model since it depends on the relative phases of the two fields (information not contained in $\mathcal{N}$) and can lead to small-scale features in the mean flow which would violate the WKB assumption of a slowly varying background. We will see that small-scale features do appear in the induced mean flow in wave-resolving simulations but that the behaviour of the waves and of the large-scale structure are well predicted by the weakly nonlinear WKB model.

5. Description of the numerical models

In this section we describe the two numerical implementations for solving the equations governing the evolution of the phase-space wave-action density and the mean flow, as well as the wave-resolving models used to validate both the WKB models and the underlying theory.

5.1. *WKB models*

The first model uses a finite-volume method to solve the Eulerian form of the phase-space wave-action-density equation (32). Wave-action density is defined on a two dimensional position-wavenumber grid while the mean flow is defined only on the position grid. The second model is a ray tracer in phase space that solves the Lagrangian form of the phase-space wave-action-density equation (34). Wave-action density is defined on a discrete set of ray points in phase space that propagate along rays defined by the phase-space-velocity field $(c_{gz}, \dot{m})$ and transport the conserved wave action density. In order to approximate the integral in the computation of the momentum flux in (35), attached to each ray point is a rectangle whose area is conserved but whose shape changes with time depending on the straining effect of the phase-space flow. For initially quasimonochromatic and spatially localized wave packets, this model is much more efficient than the Eulerian model since it need only update the solution on points with nonzero wave-action density and not on the entire phase-space domain.

5.1.1. *Eulerian model: finite-volume method*

In the Eulerian model, $\mathcal{N}(z,m,t)$ is defined on a regular grid of rectangular cells in position-wavenumber space, and the large-scale background fields $N(z)$ and $U(z,t)$ and the mean momentum flux $\overline{u'w'}(z,t)$ are defined on the position grid using the staggered arrangement shown in figure 2.

A standard fourth-order Runge-Kutta scheme (e.g. Durran 2010) is used for the time integration, with the time step dynamically adapted to satisfy a CFL condition. The flux of $\mathcal{N}$ is calculated using a second-order MUSCL upwind scheme with the MC limiter (Kemm 2010). The MUSCL scheme is stable for transport problems with sharp gradients, such as occur in the wavenumber direction near a quasimonochromatic wave packet, while being much less diffusive than a simple first-order upwind scheme in regions where the solution is smooth. The components of the phase-space-velocity field $(c_{gz}, \dot{m})$ needed to compute the fluxes of the wave-action density are calculated in each Runge-Kutta sub-step (since they depend on time through $U(z,t)$) using the ray equations (20a) and (20b).

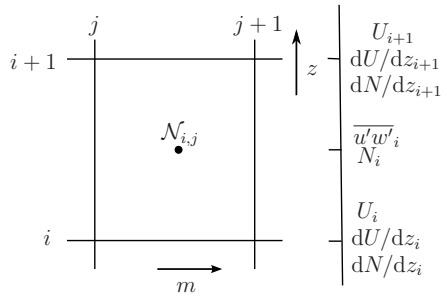

Figure 2. A finite-volume cell for the Eulerian WKB model: The grid for variables depending only on height is staggered as shown.

Equation (36) is used to calculate the time evolution of the mean flow $U(z,t)$. The total horizontal-mean momentum flux $\overline{u'w'}$ is computed at each height z by summing the integrand over the m domain, i.e.

$$\overline{u'w'}_i = -\sum_j \frac{N_i m_j k}{(k^2+m_j^2)^{\frac{3}{2}}} |k\mathcal{N}_{i,j}| \, \Delta_m \,, \qquad (38)$$

where Δ_m is the width of a grid cell in the wavenumber direction. The absolute value applied to $k\mathcal{N}_{i,j}$ ensures the correct sign of $\overline{u'w'}$ is obtained for both branches of $\Omega_\pm$. A centred difference approximation is used for the z-derivative of $\overline{u'w'}$. The mean wind is updated at each Runge-Kutta sub-step.

Periodic boundary conditions are used in the z direction, while on the boundaries in the m direction, a no-inflow condition was used, i.e. the value of $\mathcal{N}$ outside the considered domain is assumed to be zero. Since the boundaries in the m direction are *de facto* high- or low-wavenumber cut-off scales for the model, the domain should be chosen large enough that significant wave energy does not leave the system.

5.1.2. *Lagrangian model: phase-space ray tracer*

The Lagrangian model exploits the fact that wave-action density is conserved on rays in phase space so that ray particles need only be initialized in the region where the wave packet is initially localized.

In order to calculate the wave-induced mean-flow tendency using (36), the momentum flux $\overline{u'w'}$ must be integrated in spectral space (which is not trivial since $\mathcal{N}$ is only known on the discrete and irregularly distributed set of ray points). To that end, we calculate the average momentum flux in a height interval between z and $z+\Delta_z$:

$$\begin{aligned}\frac{1}{\Delta_z}\int_z^{z+\Delta_z} \overline{u'w'}\mathrm{d}z &= \frac{1}{\Delta_z}\int_{-\infty}^{\infty}\int_z^{z+\Delta_z} kc_{gz}\mathcal{N}\mathrm{d}z\mathrm{d}m \\ &= \frac{1}{\Delta_z}\int_{R\cap R_Z} kc_{gz}\mathcal{N}\mathrm{d}z\mathrm{d}m \,, \qquad (39)\end{aligned}$$

where R is the phase-space region of nonzero $\mathcal{N}$ and $R_Z = (z, z+\Delta_z)\times(-\infty,\infty)$. The region R becomes deformed in time due to the strain and shear in the phase-space flow $(c_{gz},\dot{m})$, but its area A_R is preserved because of the divergence-free property of the phase space velocity (see equation 33), i.e.

$$\begin{aligned}\frac{\mathrm{d}A_R}{\mathrm{d}t} &= \frac{\mathrm{d}}{\mathrm{d}t}\int_R \mathrm{d}z\mathrm{d}m \\ &= \oint_{\partial R} (c_{gz},\dot{m})\cdot\hat{\nu}\,\mathrm{d}l \\ &= \int_R \left(\frac{\partial c_{gz}}{\partial z}+\frac{\partial \dot{m}}{\partial m}\right)\mathrm{d}z\mathrm{d}m = 0 \,, \qquad (40)\end{aligned}$$

where ∂R is the boundary of R, $\hat{\nu}$ is the outward directed unit vector normal to R, $\mathrm{d}l$ is a line element in ∂R, and the two-dimensional version of the divergence theorem has been used. We approximate R by attaching to each ray particle a small rectangle and let one side of the rectangle (say Δm) change with time while keeping the area fixed (see figure 3). There are obviously more sophisticated

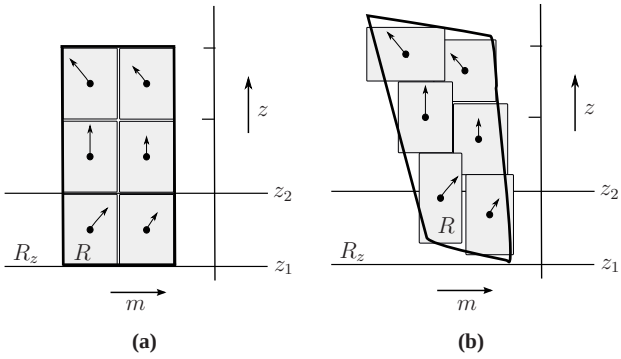

Figure 3. Schematic illustration of the area-preserving property of the phase-space flow, showing the region of nonzero wave-action density R and rectangles attached to ray particles (a) at the initial time and (b) at a later time. R is deformed by the phase-space velocity $(c_{gz},\dot{m})$ (indicated by vectors). The momentum flux in the interval (z_1,z_2) is calculated by integrating over $R\cap R_Z$.

methods for tracking the evolution of R, but none that we have tried give better results than this simple approach, which also generalizes easily to higher dimensions.

Associated with each ray particle is thus its phase space position (z,m), its conserved phase-space wave-action density $\mathcal{N}$, and the width Δm and conserved area of the phase-space rectangle attached to it. For the results presented below, two columns of ray particles, each column at a slightly different wavenumber, were initialized as shown schematically in figure 4a. Using two columns instead of one allows the distribution of ray particles to adjust in a realistic way to shear in the c_{gz} field.

The same staggered position grid as in the Eulerian model is used for U, N and $\overline{u'w'}$. For each ray particle, the integral in (39) is evaluated analytically over the portion of the attached rectangle contained within each interval in the fixed U grid (see figure 4b):

$$\begin{aligned}\overline{u'w'}^{(i)}_{ray} &= -\left(\frac{\Delta z_i}{\Delta z}\right)\int_{m_1}^{m_2}\frac{N_i k m}{(k^2+m^2)^{\frac{3}{2}}}|k\mathcal{N}|\mathrm{d}m \\ &= \left(\frac{\Delta z_i}{\Delta z}\right)N_i k|k\mathcal{N}|\left[\frac{1}{(k^2+m_2^2)^{\frac{1}{2}}}-\frac{1}{(k^2+m_1^2)^{\frac{1}{2}}}\right] \,, \qquad (41)\end{aligned}$$

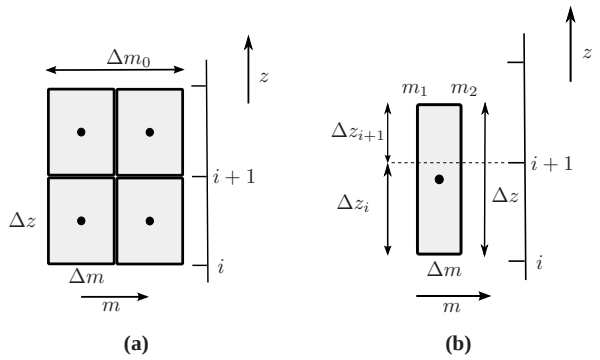

Figure 4. Schematic illustration of the momentum-flux calculation using the phase-space ray tracer: (a) initial position of ray particles and rectangles; (b) partition of a rectangle at a later time so that the mean momentum flux due to the portion of the rectangle lying within each grid cell is computed separately.

where $m_1 = (m - \frac{\Delta m}{2})$, $m_2 = (m + \frac{\Delta m}{2})$, and $\Delta z_i/\Delta z$ is the fraction of the rectangle contained within the i-th interval on the fixed grid. The resulting $\overline{u'w'}^{(i)}_{ray}$ is added to the corresponding element $\overline{u'w'}_i$ in the fixed grid array. Once the momentum flux due to all ray particles has been accounted for, a simple running average filter with window width $\Delta_{\rm smooth}$ of three grid cells is applied to $\overline{u'w'}$ to remove small-scale features arising due to the coarseness of the ray-particle distribution, and then the mean flow tendency is computed from (36) using a centred difference approximation to the z derivative (as in the Eulerian model).

The time evolution of z and m is computed using (20a) and (20b), in Lagrangian form:

$$\frac{D_r z}{Dt} = \mp \frac{Nkm}{(k^2+m^2)^{\frac{3}{2}}} \equiv c_{gz} \ , \tag{42a}$$

$$\frac{D_r m}{Dt} = \mp \frac{k}{\sqrt{k^2+m^2}} \frac{\mathrm{d}N}{\mathrm{d}z} - k\frac{\partial U}{\partial z} \equiv \dot{m} \ , \tag{42b}$$

and that of Δm using

$$\frac{D_r}{Dt}(\Delta m) = \dot{m}(m_2, z) - \dot{m}(m_1, z) \ . \tag{43}$$

Values of N, $\mathrm{d}N/\mathrm{d}z$ and $\mathrm{d}U/\mathrm{d}z$ at ray-particle positions are obtained by linear interpolation from the respective values on the fixed grid. Again the standard fourth-order Runge-Kutta scheme is used for the time integration.

Periodic boundary conditions are used in the z direction, i.e. ray particles leaving the top of the domain reenter through the bottom. No boundary conditions are needed in the m direction in this model.

5.2. *Validation models*

For validation of the WKB models we use both a one-dimensional model that solves the weakly nonlinear Boussinesq equations for a wave field with constant horizontal wavenumber k and a fully nonlinear large-eddy-simulation model for solving the Boussinesq equations in two dimensions.

5.2.1. *Weakly nonlinear wave-resolving model (WNL)*

The one-dimensional weakly nonlinear model solves the system (3) assuming a perturbation field of the form

$$\begin{pmatrix} u'(x,z,t) \\ w'(x,z,t) \\ b'(x,z,t) \\ p'(x,z,t) \end{pmatrix} = \Re \left\{ \begin{pmatrix} \hat{u}'(z,t) \\ \hat{w}'(z,t) \\ \hat{b}'(z,t) \\ \hat{p}'(z,t) \end{pmatrix} e^{ikx} \right\} \ , \tag{44}$$

where $\hat{u}'$, $\hat{w}'$, $\hat{b}'$ and $\hat{p}'$ are complex height- and time-dependent fields, coupled to the equation for the mean flow:

$$\frac{\partial U}{\partial t} = -\frac{1}{4}\frac{\partial}{\partial z}\left(\hat{u}'\hat{w}'^* + \hat{u}'^*\hat{w}'\right) \ . \tag{45}$$

The pressure is computed by solving the Poisson equation obtained from setting the divergence of the velocity tendency to zero.

The model uses a staggered grid with the vertical-wind perturbation defined on the grid-cell boundaries and the horizontal-wind, pressure and buoyancy perturbations defined at the grid-cell centres. The Brunt-Väisälä frequency N and the mean flow U are also defined at the grid-cell centres. The usual fourth-order Runge-Kutta scheme is used for the time integration, and centred finite differences for the spatial derivatives. The discrete Fourier transform is used to solve the Poisson equation for the pressure at every Runge-Kutta sub-step.

Some explicit kinematic viscosity ν and thermal diffusivity μ are required for stability of the model. For all simulations, both are set to 10^{-2} m^{2}s^{-1} (a typical value for the stratopause region). Dissipation has little effect on the gravity waves studied here, which have wavelengths of a few kilometres (the time scale of viscous decay $(\nu k^2)^{-1} >$ 10 days is long compared to the simulation times of less than a day).

5.2.2. *Fully nonlinear large-eddy-simulation model (INCA)*

The other validation model is the large-eddy-simulation model INCA (http://www.inca-cfd.org) which solves the fully nonlinear Boussinesq equations (1) using the adaptive local deconvolution method (ALDM) (Hickel *et al.* 2006) as subgrid-scale-turbulence parameterization. See Remmler and Hickel (2012, 2013) for a detailed model description and validation of the LES scheme against direct numerical simulations of weakly and strongly stratified flow. For consistency, the same explicit viscosity and diffusion parameters are used as in the weakly nonlinear model.

The use of the fully nonlinear model also serves as a reference to validate the weakly nonlinear theory on which the WKB analysis is based, i.e. to test how well the weakly nonlinear dynamics, which neglect wave-wave interactions, can describe the propagation of wave packets in a time- and space-dependent background flow and their interaction with the background flow.

6. Numerical results

The WKB and validation models were used to simulate the propagation of an initially quasimonochromatic wave

packet with the z-dependent buoyancy amplitude

$$A_b(z) = a_0 \frac{N_0^2}{m_0} \exp\left[-\frac{(z-z_0)^2}{2\sigma^2}\right] , \tag{46}$$

i.e. a Gaussian envelope centred at z_0 and with half-width σ. N_0 is the local Brunt-Väisälä frequency at $z = z_0$ and m_0 is the initial vertical wavenumber of the wave packet. The nondimensional amplitude a_0 is defined so that the threshold criterion for static stability, $N^2 + \partial b/\partial z > 0$, will be satisfied everywhere in the wave packet if $a_0 < 1$. The polarization relations (10) imply the following initial perturbation fields for the wave-resolving validation models:

$$b'(x,z,t_0) = A_b(z)\cos(kx + m_0 z) , \tag{47a}$$

$$u'(x,z,t_0) = A_b(z)\frac{m_0}{k}\frac{\hat{\omega}_0}{N_0^2}\sin(kx + m_0 z) , \tag{47b}$$

$$w'(x,z,t_0) = -A_b(z)\frac{\hat{\omega}_0}{N_0^2}\sin(kx + m_0 z) , \tag{47c}$$

where $\hat{\omega}_0$ is the intrinsic frequency of the initially quasimonochromatic wave packet. Note that due to the z-dependent amplitude of w', the initial condition (47) does not satisfy the nondivergence constraint (1d). In all wave-resolving simulations, the $\mathcal{O}(\epsilon)$ divergent part is removed before the first time step. The initial wave-energy density is, using (10),

$$\begin{aligned} E(z,t_0) &= \frac{1}{2}\overline{\left[u'^2(x,z,t_0) + w'^2(x,z,t_0) + \frac{b'^2(x,z,t_0)}{N_0^2}\right]} \\ &= \frac{A_b^2(z)}{2N_0^2} . \end{aligned} \tag{48}$$

In the WKB models, the choice of the initial wave-action density corresponding to (48) is not unique. All that is required is that the integral of $\hat{\omega}\mathcal{N}$ over m equal E. The definition (25) calls for a delta function (a truly quasimonochromatic wave packet), a discrete approximation to which is

$$\mathcal{N}(z,m,t_0) = \begin{cases} \dfrac{A_b^2(z)}{2N_0^2\hat{\omega}}\dfrac{1}{\Delta m_0} , \\ \quad \text{if } m_0 - \frac{\Delta m_0}{2} < m < m_0 + \frac{\Delta m_0}{2} \\ 0 , \quad \text{otherwise} \end{cases} , \tag{49}$$

where Δm_0 is a small wavenumber interval. We generally took Δm_0 to be the width of a single finite-volume cell in the Eulerian WKB model. A measure of the sensitivity to the width of the wavenumber interval is the relative variation of the group speed across the interval

$$\begin{aligned} \frac{\Delta c_{gz}}{c_{gz}(m_0)} &\approx \frac{1}{c_{gz}(m_0)}\left.\frac{\partial c_{gz}}{\partial m}\right|_{m_0}\Delta m_0 \\ &= \left(1 - \frac{3m_0^2}{m_0^2 + k^2}\right)\frac{\Delta m_0}{m_0} . \end{aligned} \tag{50}$$

It follows that when $\Delta m_0/m_0$ is small, the patch of nonzero $\mathcal{N}$ initially moves with approximately uniform group speed and relatively little spurious dispersion is introduced. In the experiments presented here, the exact value of Δm_0 does not make much difference as long as it is much smaller than m_0. A convenient by-product of the region of nonzero $\mathcal{N}$ having a finite width is that the energy density can never become infinite, for example at a reflecting level (see section 6.4 and appendix B) unlike in conventional ray-tracing in physical space.

We conducted a set of experiments in which the gravity-wave packet propagates through different large-scale background fields: an initially uniform background, a background with varying stratification, a weak wind jet, and a wave-reflecting wind jet. The physical parameters used for the various experiments are summarized in Table 1 and the model parameters in Table 2.

Each simulation was done both with no initial mean flow at the position of the wave packet ("case 1") and with an initial mean flow that, to leading order, propagates together with the wave packet (Acheson 1976; Sutherland 2006b), *viz.*

$$U_{ind}(z,t_0) = kA(z,t_0) = k\frac{A_b^2(z)}{2N^2\hat{\omega}} \tag{51}$$

("case 2"). It follows from (18) that in the weakly nonlinear limit, U_{ind} remains equal to the wave pseudomomentum kA. While the inclusion of the initial wave-induced mean flow is preferred by some authors, we will see that at later times, in the upper part of the domain (where $U_{ind}(t_0) = 0$) there is little difference between the simulations with and without an initial wave-induced mean flow. This is to be expected from (18), which says that the local mean-flow tendency depends only on the local wave pseudomomentum tendency and not directly on the large-scale structure of the U field.

The two diagnostic quantities we will use to compare the WKB and validation models are the mean flow $U(z,t)$ and the wave-1 energy density E. For the WKB models, E is calculated by integrating the intrinsic frequency times the wave-action density over the wavenumber domain:

$$E_{WKB} = \int \mathcal{N}\hat{\omega}\,\mathrm{d}m , \tag{52}$$

for the weakly nonlinear validation model, it is

$$E_{WNL} = \frac{1}{4}\left(|\hat{u}'|^2 + |\hat{w}'|^2 + \frac{|\hat{b}'|^2}{N^2}\right) , \tag{53}$$

and for the fully nonlinear model, it is the horizontally-averaged energy density contained in the first horizontal Fourier mode of the velocity and buoyancy fields.

6.1. *Hydrostatic wave packet propagating through a uniform background*

First we consider a wave packet propagating through a uniform stratification with $N(z) = N_0 = 0.02$ s^{-1}. The waves are "hydrostatic" with horizontal wavelength $\lambda_x = 30$ km and initial vertical wavelength $\lambda_{z0} = 3$ km ($k = 2.1 \times 10^{-4}$ m^{-1} and $m_0 = -2.1 \times 10^{-3}$ m^{-1}). The wave packet has half-width $\sigma = 5$ km and is initially centered at $z_0 = 30$ km. The spatial domain has a total height of $l_z = 100$ km. We consider wave packets with amplitudes a_0 of 0.1, 0.5 and 0.8.

For the Eulerian WKB model a wavenumber domain of -0.007 m$^{-1} < m < -0.0005$ m^{-1} was used, with $n_z = 500$ cells in the z direction and $n_m = 70$ in the m direction. The initial wave-action-density distribution had width in

Test case	Background	Wave packet	Domain size and run time
Hydrostatic wave packet in a uniform background	$N_0 = 2 \times 10^{-2}$ s^{-1}	$\lambda_x = 30$ km, $\lambda_{z0} = 3$ km $k = 2\pi/\lambda_x$, $m_0 = -2\pi/\lambda_{z0}$ $\omega = \Omega_+$ $\sigma = 5$ km, $z_0 = 30$ km $a_0 = 0.1,\ 0.5,\ 0.8$	$l_x = 30$ km $l_z = 100$ km $t_{\max} = 800$ min
Variable stratification	$N_0 = 2 \times 10^{-2}$ s^{-1} $a_{back} = 0.8$ $M = 2\pi/(20\ \text{km})$ $z_1 = 50$ km	$\lambda_x = 30$ km, $\lambda_{z0} = 3$ km $k = 2\pi/\lambda_x$, $m_0 = -2\pi/\lambda_{z0}$ $\omega = \Omega_+$ $\sigma = 5$ km, $z_0 = 30$ km $a_0 = 0.5$	$l_x = 30$ km $l_z = 100$ km $t_{\max} = 800$ min
Wind jet	$N_0 = 2 \times 10^{-2}$ s^{-1} $U_0 = 20$ m s^{-1} $z_1 = 50$ km $\Sigma_U = 3$ km	$\lambda_x = 30$ km, $\lambda_{z0} = 3$ km $k = 2\pi/\lambda_x$, $m_0 = 2\pi/\lambda_{z0}$ $\omega = \Omega_-$ $\sigma = 5$ km, $z_0 = 20$ km $a_0 = 0.5$	$l_x = 30$ km $l_z = 100$ km $t_{\max} = 800$ min
Reflecting jet	$N_0 = 2 \times 10^{-2}$ s^{-1} $U_0 = 5$ m s^{-1} $z_1 = 70$ km $\Sigma_U = 3$ km	$\lambda_x = 3$ km, $\lambda_{z0} = 3$ km $k = 2\pi/\lambda_x$, $m_0 = 2\pi/\lambda_{z0}$ $\omega = \Omega_-$ $\sigma = 5$ km, $z_0 = 40$ km $a_0 = 0.2$	$l_x = 3$ km $l_z = 100$ km $t_{\max} = 300$ min
Modulationally unstable wave packet (s)table, (m)etastable, (u)nstable	$N_0 = 2 \times 10^{-2}$ s^{-1}	$\lambda_x = 2$ km $\lambda_{z0} = 1.4^{(\text{s})},\ 2.9^{(\text{m})},\ 5^{(\text{u})}$ km $k = 2\pi/\lambda_x$, $m_0 = -2\pi/\lambda_{z0}$ $\omega = \Omega_+$ $\sigma = 3.2$ km, $z_0 = 30$ km $a_0 = 0.12^{(\text{s})},\ 0.21^{(\text{m})},\ 0.42^{(\text{u})}$	$l_x =$ N/A* $l_z = 50$ km $t_{\max} = 200$ min

Table 1. Summary of test case parameters. Refer to equations (46), (47), (54), and (56) for the forms of the wave packet, background buoyancy perturbation and background jet. $t_{\max}$ is the total model time of the simulations. *The fully nonlinear model was not run for the modulational instability experiment.

Eulerian WKB (finite-volume method)	Lagrangian WKB ("ray tracer")	Validation models	
		Weakly nonlinear	LES ("INCA")
(U, S, J) $m \in [-.007, -.0005]$ m^{-1} $n_z \times n_m = 500 \times 70$ (R) $m \in [-.01, .005]$ m^{-1} $n_z \times n_m = 500 \times 140$ (MI) $m \in [-.012, .002]$ m^{-1} $n_z \times n_m = 500 \times 140$ $(\Delta t)_{\max} = 1$ s $CFL = 0.5$ $\Delta m_0 = 10^{-4}$ m^{-1}	$\Delta m_0 = 10^{-4}$ m^{-1} $n_z = 500$ $n_{\text{ray}} = 2 \times 200$ (U, S, J, R) $\Delta_z = 200$ m $\Delta_{\text{smooth}} = 600$ m (MI) $\Delta_z = 100$ m $\Delta_{\text{smooth}} = 300$ m $\Delta t = 1$ s	$\nu = \mu = 10^{-2}$ m^{2}s^{-1} $n_z = 2048$ (U, S, J, R) $\Delta_z \approx 50$ m (MI) $\Delta_z \approx 25$ m $\Delta t = 1$ s	$n_x \times n_z = 64 \times 2048$ (U, S, J) $\Delta_x \times \Delta_z = 470$ m $\times$ 50 m (R) $\Delta_x \times \Delta_z = 47$ m $\times$ 50 m $CFL = 0.5$ $\nu = \mu = 10^{-2}$ m^{2}s^{-1} (MI) no LES simulations

Table 2. Summary of model-configuration parameters (U = uniform background; S = variable stratification; J = background jet; R = reflecting jet; MI = modulationally unstable wave packet). Δ_x and Δ_z are the grid-cell sizes in the various models and Δt is the time step (where applicable). CFL is the CFL number appropriately defined for the Eulerian WKB and fully nonlinear LES models. In the Eulerian WKB model the time step is the smaller of $(\Delta t)_{\max}$ and the time step determined by the CFL condition.

the wavenumber direction equivalent to one grid cell, or $\Delta m_0 = 10^{-4}$ m^{-1}. For the ray tracer, the ray particles in each of the two columns were initialized at equally spaced intervals between $z = 10$ km and $z = 50$ km and at $m = m_0 - \Delta m_0/2$ and $m = m_0 + \Delta m_0/2$. The total number of rays was $n_{\mathrm{ray}} = 2 \times 200$. The same resolution in z for the large-scale fields was used as in the Eulerian model (so that there was exactly one ray particle in each column per interval on the fixed grid). The wave-resolving weakly nonlinear model used $n_z = 2048$ points while the fully nonlinear model was run in a domain of width $l_x = 30$ km (one horizontal wavelength) with $n_x \times n_z = 64 \times 2048$ grid cells. Figure 5 shows the initial wave-action density in the WKB models and the initial buoyancy field at $x = 0$ in the wave-resolving models.

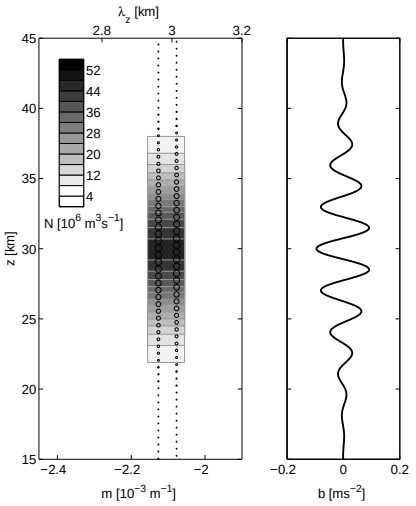

Figure 5. Initial condition for the $a_0 = 0.5$ case of the hydrostatic wave packet in a uniform background. Left: phase-space wave-action density $\mathcal{N}$ in the WKB finite-volume model and ray-particle distribution in the WKB ray tracer (circles; size proportional to $\mathcal{N}$). Right: initial buoyancy at $x = 0$ in the wave-resolving models.

The mean momentum flux $\overline{u'w'}$ initially has the same Gaussian profile as the wave-action density. It therefore decelerates the mean flow on the lower flank and accelerates it on the upper flank. Figure 6 shows near perfect agreement between the induced mean flows and wave-energy densities simulated by the WKB models and the wave-resolving models after 200 minutes. In case 1 (panels a, b and d) this generates a dipolar background shear flow in the early part of the simulation. In case 2 (panel c), by construction, the momentum flux acts to propagate the initial background flow perturbation upward with the wave packet so no negative mean flow is left behind in the wake of the wave packet. As pointed out by Dosser and Sutherland (2011), the negative mean flow in case 1 is exactly equal to the negative of the initial wave pseudomomentum. In both cases 1 and 2 the total horizontal momentum is conserved.

Since the stratification is uniform, (20b) implies that changes in wavenumber depend only on the shear in the mean flow. Therefore, in case 1, $\dot{m}$ becomes positive on the lower and upper flanks of the wave packet and negative in the middle, deflecting the wave-action density signal to less negative wavenumbers (longer wavelengths) and more negative wavenumbers (shorter wavelengths), respectively. In case 2, the shear already present in the initial background flow affects $\dot{m}$ and the $\mathcal{N}$ distribution accordingly. This is illustrated for the case $a_0 = 0.5$ in figure 7. Note that as expected, the mean flow in the upper part of the domain – above 35 km – is very similar in cases 1 and 2.

For comparison, the energy density from a purely linear wave-resolving simulation (without the wave-induced mean flow) is also plotted in figure 6. As pointed out by Fritts and Dunkerton (1984), one effect of the induced mean flow is to broaden the wave packet and to reduce its peak amplitude. This comes about because, for hydrostatic wave packets, the mean flow changes the vertical wavenumber, and hence the vertical group speed, in such a way as to accelerate the leading flank and decelerate the trailing flank (this is not the case for very nonhydrostatic wave packets, cf. section 6.5). Fritts and Dunkerton (1984) also found that the interaction between the wave packet and its wave-induced mean flow can lead to "dislocated critical levels" that cannot be explained with linear theory. As one would expect, the departure of the weakly nonlinear solutions from the prediction of linear dynamics increases with wave packet amplitude. The $a_0 = 0.1$ simulations induce only very weak shear in the background flow and thus very little change to the group velocity distribution in the wave packet, which therefore remains close to Gaussian (figure 6a).

Caustics develop during the later evolution of the wave field in both cases 1 and 2. Figure 8 shows the positions of the ray particles after 500 minutes in the simulations with $a_0 = 0.5$, with a curve drawn connecting initially adjacent ray particles. Caustics occur wherever a horizontal line would intersect the curve more than once, indicating that there is nonzero wave amplitude at more than one wavenumber at the same height (i.e. rays in physical space are crossing). In the figure this can be seen in the lower part of the wave packet in case 1 and in the upper part in case 2, where initially lower placed particles have overtaken initially higher placed particles.

The similarity between the results obtained with the weakly nonlinear and the fully nonlinear models supports the claim of Sutherland (2006b) that the propagation of a horizontally periodic, vertically compact wave packet can be represented well as long as the interaction between the waves and the mean flow is accounted for. Higher harmonics of the waves do not play a significant role.

6.2. *Wave packet propagation through a stationary buoyancy field*

In the next experiment, the wave packet propagates through a variable background stratification associated with the buoyancy field $N_0^2 z + B(z)$, where

$$B(z) = \begin{cases} \dfrac{a_{back} N_0^2}{M} \left[1 - \cos\left(M(z - z_1)\right)\right] , \\ \qquad \text{if } z_1 \le z \le z_1 + 2\pi/M \\ 0 , \qquad \text{otherwise} \end{cases} , \quad (54)$$

which may be interpreted as the zero-frequency limiting case of a long-wavelength resolved gravity-wave packet through which the waves parameterized using WKB theory propagate. The background perturbation $B(z)$ has lower limit $z_1 = 50$ km, vertical wavenumber $M = 2\pi/(20\ \mathrm{km})$, and a nondimensional amplitude $a_{back} = 0.8$ (again defined relative to the threshold for static stability). In this case the total Brunt-Väisälä frequency is given by $N(z) = \sqrt{N_0^2 + \mathrm{d}B/\mathrm{d}z}$. In the WKB models, both N and $\mathrm{d}N/\mathrm{d}z$

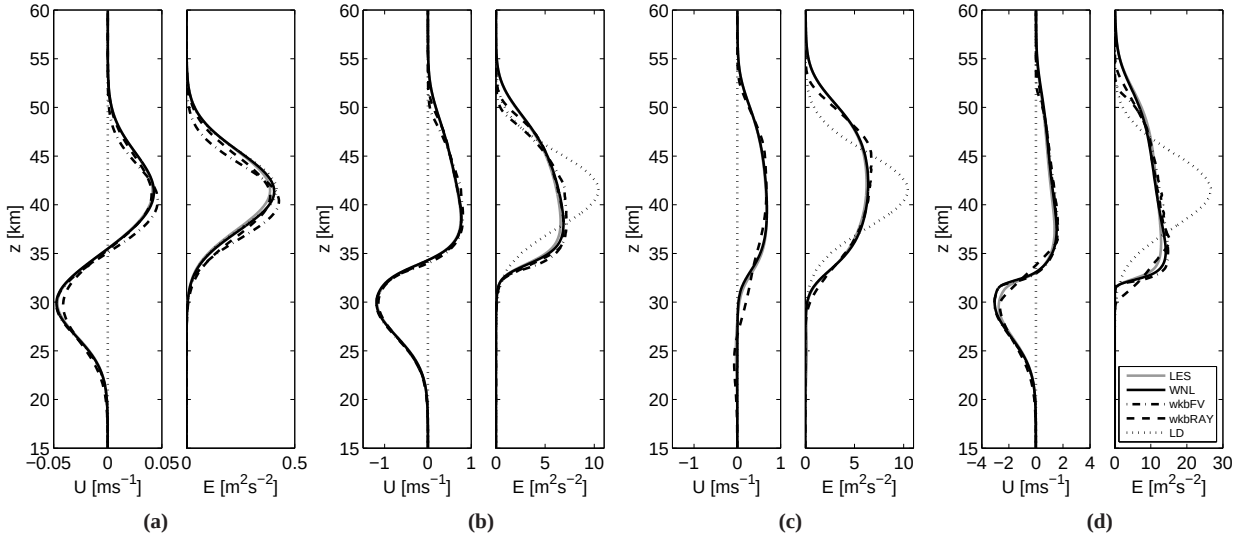

Figure 6. Mean flow (left) at $t = 200$ minutes induced by the wave packet propagating through an initially uniform background and the corresponding horizontal-mean wave-energy density (right) simulated by all four models. (a) Wave packet amplitude $a_0 = 0.1$ case 1; (b) $a_0 = 0.5$ case 1; (c) $a_0 = 0.5$ case 2; (d) $a_0 = 0.8$ case 1. (LES: fully nonlinear wave-resolving model; WNL: weakly nonlinear wave-resolving model; wkbFV: Eulerian WKB finite-volume model; wkbRay: WKB ray tracer; LD: linear dynamics).

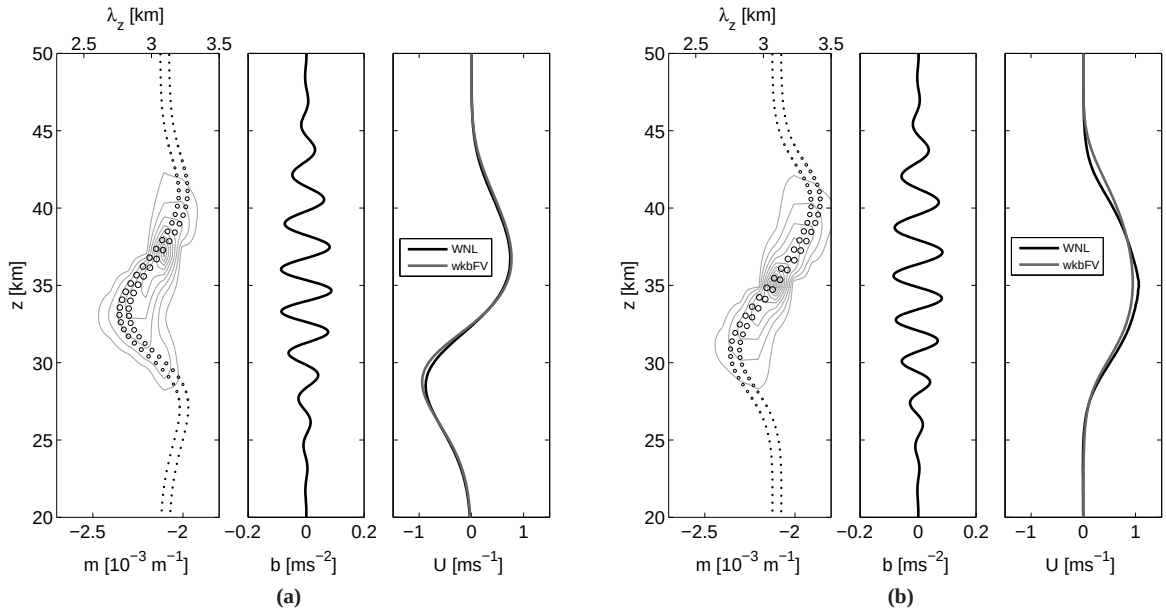

Figure 7. Snapshot at $t = 100$ minutes of the wave packet with initial amplitude $a_0 = 0.5$ propagating through a uniform background in (a) case 1 and (b) case 2. Contours in the left panels show the wave-action density from the Eulerian WKB model (contour interval 5×10^6 m^3 s^{-1}) and the circles indicate the positions of the ray particles in the Lagrangian WKB model (size proportional to $\mathcal{N}$). Centre panels show a cross-section of buoyancy at $x = 0$ from the weakly nonlinear model. Right panels show the mean flow from the Eulerian WKB model (grey) and the weakly nonlinear model (black).

are computed analytically from (54) and stored on the grid as shown in figure 2.

Based on simple addition, one might expect that if $a_{back} + |a_0| > 1$, when the wave packet reaches the level of minimum static stability in the background, it will become statically unstable. Perhaps counterintuitively, however, one can show (see appendix A) that the wavelength and amplitude of the waves change in such a way that the minimum total static stability occurs as the centre of the wave packet reaches the point of *maximum* static stability in the background. For the hydrostatic waves used here, as $a_{back} \to 1$ then $|a_0|$ would have to be at least 0.76 for the possibility of static instability occurring (for details see equation 64 in appendix A). However, in a more general case with feedback from the waves on the large-scale flow, the interaction of a statically stable wave packet with a statically stable background is unlikely to lead to static instability.

Figure 9 shows the distribution of wave-action density predicted by the WKB models as the wave packet moves through the background buoyancy perturbation. The deflection of the wave packet in this region is dominated by the derivative of $N(z)$, so there is little difference between cases 1 and 2 in this experiment. As in the first experiment,

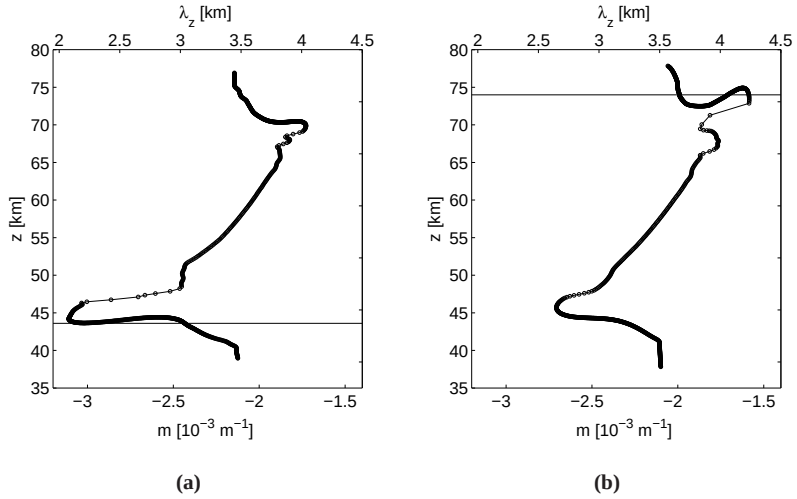

Figure 8. Distribution of ray particles at $t = 500$ minutes from the experiment with the wave packet with $a_0 = 0.5$ propagating through a uniform background for (a) case 1 and (b) case 2. Examples of caustics are indicated by the horizontal lines intersecting the curves connecting the ray particles.

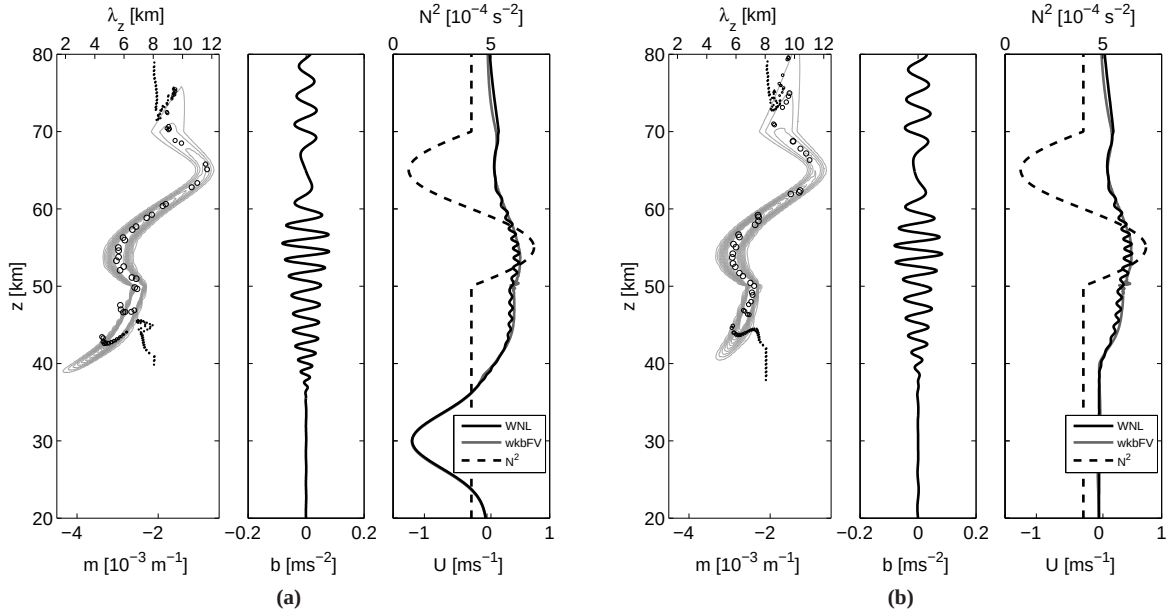

Figure 9. As in figure 7 but at $t = 500$ minutes in the test case with a variable background stratification. The dashed line in the right panels shows the total N^2 (with values indicated on the upper horizontal axis). The contour interval for the wave-action density (left panels) is 5×10^5 m^3 s^{-1}.

caustics can be observed on the upper and lower flanks of the wave packet in both cases.

Figure 10 shows the wave-packet energy density as a function of height and time for case 2 from all models. Before it interacts with the large-scale buoyancy perturbation, the wave packet propagates vertically, slightly perturbed by the induced mean flow as in the previous experiment. As the waves interact with the large-scale buoyancy field and their wavenumber changes, the wave-packet energy density also changes so as to globally conserve wave action. This may be most easily understood if we for the moment neglect the time-dependent background wind. In that case (as is shown in appendix A), the physical-space wave-action density A at the centre of the wave packet $z_c(t)$ is inversely proportional to the vertical group velocity. Since in this experiment the wave packet is almost hydrostatic (i.e. $|k| \ll |m|$), its vertical group velocity and intrinsic frequency satisfy

$$\hat{\omega} \approx \frac{Nk}{|m|}\,, \quad c_{gz} \approx \frac{Nk}{|m|^2}\,. \tag{55}$$

It can be seen in figure 9 that $|m|$ is reduced as the wave packet passes through the region of reduced N^2. From (55), $A(z_c) \propto c_{gz}^{-1} \approx |m|/\hat{\omega}$ and therefore the wave energy at the centre of the wave packet $E(z_c) \propto |m|$ is also reduced. The presence of the weak wave-induced mean flow alters this picture only slightly.

Figure 11 shows the wave-induced mean flow U from case 2 as a function of height and time. Where the wave energy is small, there is (as one would expect) almost no momentum transfer to the mean flow. Also shown in the figure is a comparison between U and the pseudomomentum P at $t = 500$ minutes from the

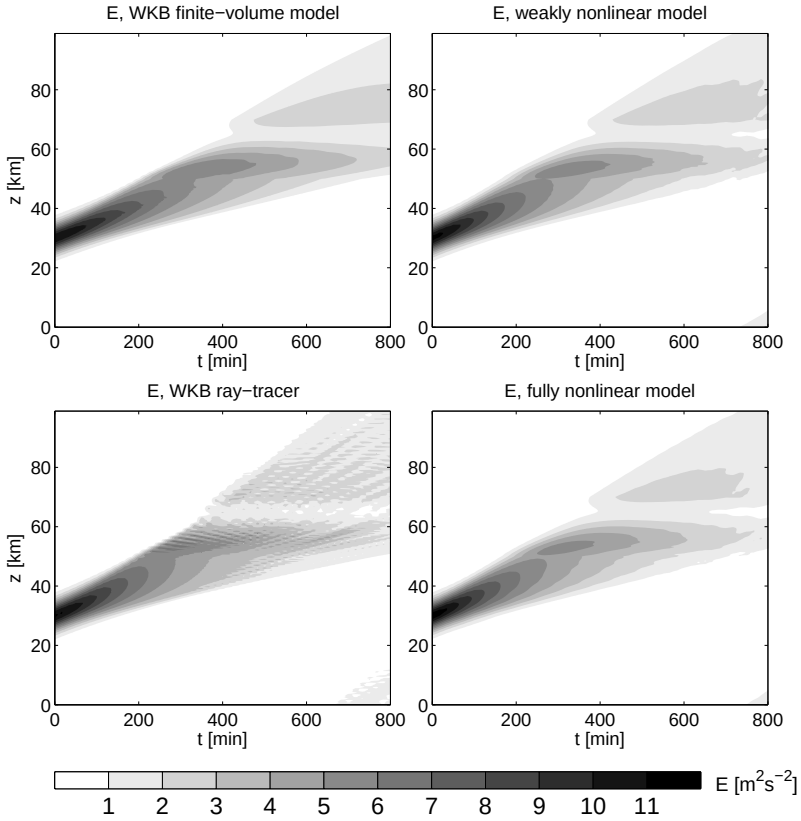

Figure 10. Horizontally averaged wave energy density versus time and height for the test case with variable stratification (for case 2).

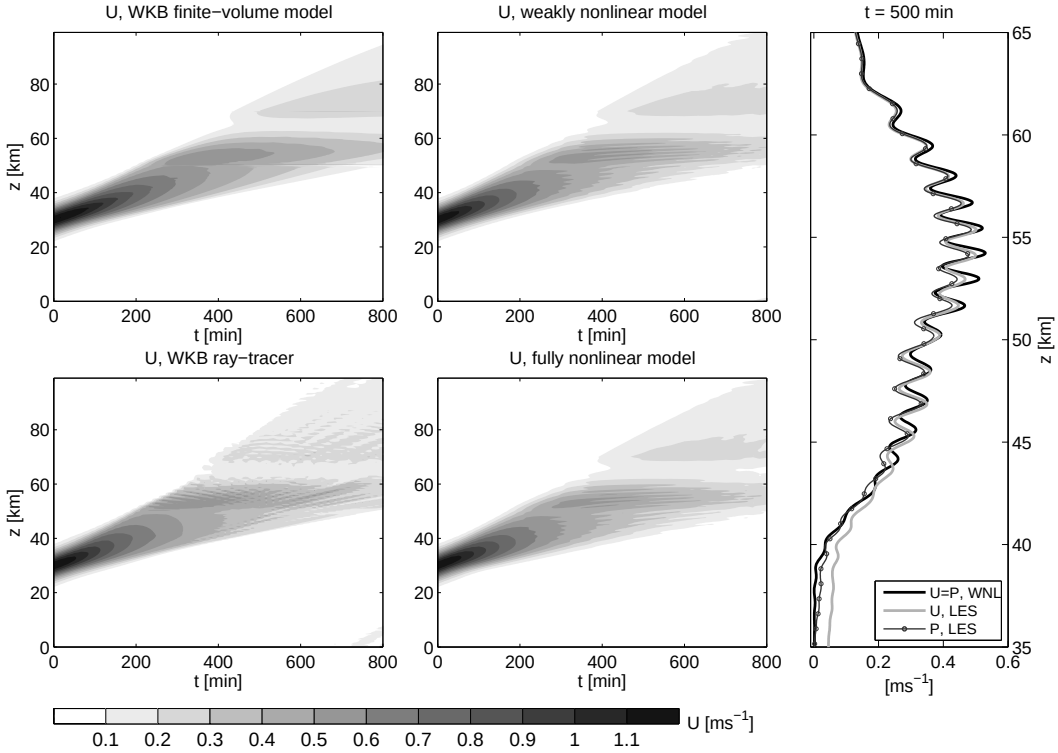

Figure 11. Mean flow U for all models from the test case with varying stratification (for case 2). Right panel shows the pseudomomentum P from the wave-resolving models at $t = 500$ minutes.

wave-resolving simulations (calculated using (19)). The equality (18) is satisfied by construction for the weakly-nonlinear model, while for the fully nonlinear model the correspondence is very close.

The mean flows produced by the two validation models are almost identical. The most striking difference between the results from the WKB and validation models is the presence of small-scale structures in U and E in the wave-resolving models. These are probably due to wave-wave–mean-flow interactions (of the sort discussed at the end of section 4) which begin to occur as the phase-space wave-action density becomes spread out in the wavenumber dimension. Since the WKB models do not account for any wave-wave interactions, they cannot reproduce these features.

6.3. *Wave packet propagation through a wind jet*

Next we consider the case where a "hydrostatic" gravity wave packet propagates through a horizontal wind jet. The wave packet is the same as in the previous cases except that it is initially centred at $z_0 = 20$ km. The background wind has the initial profile

$$U_{jet}(z) = U_0 \operatorname{sech}\left[\frac{(z-z_1)^2}{\Sigma_U^2}\right], \tag{56}$$

with $z_1 = 50$ km, $U_0 = 20$ m s^{-1} and $\Sigma_U = 3$ km. The jet profile and wave packet are chosen so that the wave packet does not encounter a critical level, where U equals the horizontal phase speed of the waves. Since the jet is positive, the horizontal phase velocity of the wave packet is therefore chosen to be negative by taking the negative root in (9), i.e. $\omega = \Omega_-$, and a positive initial vertical wavenumber m_0.

The jet refracts the wave packet in much the same way as does the variable stratification in the previous experiment. Figure 12 shows the energy density for case 1 as a function of height and time. Again, it can be explained in terms of the wavenumber velocity $\dot{m}$. As the waves propagate through the lower flank of the jet, the vertical wavenumber becomes smaller due to the wind shear, simultaneously reducing the wave packet energy density. Figure 13 shows good agreement between the induced mean flow, i.e. $U(z,t) - U_{jet}(z)$, from case 1 simulated by the WKB models and the wave-resolving models after 500 minutes, as the wave packet passes through the peak of the jet. There are again small-scale structures in U in the wave-resolving models, but they do not seem to affect the wave energy above the jet. Notice that the mean flow "left behind" in the wake of the wave packet has positive sign in this case because the horizontal phase speed, and hence the pseudomomentum, of the wave packet is negative.

This is the only experiment in which there is a large difference between the weakly nonlinear and fully nonlinear wave-resolving models. In the region of the jet, the wave energy in the weakly nonlinear model (and the WKB models) is strongly reduced and there is almost no momentum transfer to the mean flow, while in the fully nonlinear model there is a significant induced mean flow (which is nevertheless of much smaller amplitude than the background jet).

Figure 14 shows the phase-space wave-action-density distribution from cases 1 and 2 also at $t = 500$ minutes. Caustics occur again on the upper and lower flanks of the wave packet in both cases. In this experiment too there is little qualitative difference between cases 1 and 2.

6.4. *Reflection by a wind jet*

If the wind jet is strong enough, WKB theory predicts that, notwithstanding the violation of the scale separation assumption, the vertical wavelength of the waves tends to infinity before the vertical wavenumber changes sign (see, e.g., Sutherland 2010), i.e. the wave packet is reflected.

Assume for simplicity a uniform stratification and (for the moment) a steady horizontal mean flow. As the waves propagate, the vertical wavenumber adjusts in such a way as to keep the frequency, given by the dispersion relation (11), constant. Reflection occurs if m passes through zero, i.e., if

$$U_0 \geq \frac{N}{k}\left(1 - \frac{k}{\sqrt{k^2+m_0^2}}\right), \tag{57}$$

where m_0 is the vertical wavenumber of the waves before they encounter the jet.

We consider this time a "non-hydrostatic" wave packet with wavelengths $\lambda_x = 3$ km and $\lambda_{z0} = 3$ km, half-width $\sigma = 5$ km, and centre initially at $z_0 = 40$ km. To avoid modulational instability as the vertical wavelength becomes large (discussed in section 6.5), the relatively low initial amplitude $a_0 = 0.2$ is chosen. Again the horizontal phase speed is chosen to be negative to exclude the possibility of a critical level. For these simulations, the jet is again of the form (56), but is centred at $z_1 = 70$ km and has a peak velocity of $U_0 = 5$ m s^{-1} (equation (57) predicts reflection if $U_0 \geq 2.8$ m s^{-1}).

To accommodate the reflection of the waves, the Eulerian WKB model required a larger wavenumber domain (straddling the $m = 0$ line) chosen to be -0.01 m$^{-1} < m < 0.005$ m^{-1} with $n_m = 140$ grid points.

Figure 15 compares the wave energy for case 1 obtained with the WKB and wave-resolving models. The WKB models are able to accurately simulate the reflection of the wave packet. Figure 16 shows the phase-space wave-action density and ray particle distributions 140 minutes after the wave packet was launched. Again there is little difference between cases 1 and 2. Figure 17 shows good agreement between the induced mean flow simulated by all models far from the reflecting level. In the region where the incident and reflected waves overlap, both wave-resolving models produce an obvious small scale signal in the induced mean flow that is not predicted by the WKB models.

The linear, steady-state version of this test case admits an analytic solution, detailed in appendix B, which can be compared to the results of simulations with the WKB and wave-resolving models (in linear mode). To approximate a steady wave-train, a much longer wavepacket with initial buoyancy amplitude

$$A_b(z) = \frac{a_0}{2}\frac{N_0^2}{m_0}\left(\tanh\frac{z-z_0+\sigma}{\beta} - \tanh\frac{z-z_0-\sigma}{\beta}\right), \tag{58}$$

where $z_0 = 80$ km, $\sigma = 65$ km and $\beta = 2$ km (essentially a smooth boxcar function between $z = 20$ km and $z = 150$ km) was used, the jet was moved up to $z_1 = 170$ km, and the height of the domain was increased to accomodate the jet and the wide wave packet. The idea was to see that wave energy does not steadily accumulate near the reflecting level. For this experiment the feedback on the

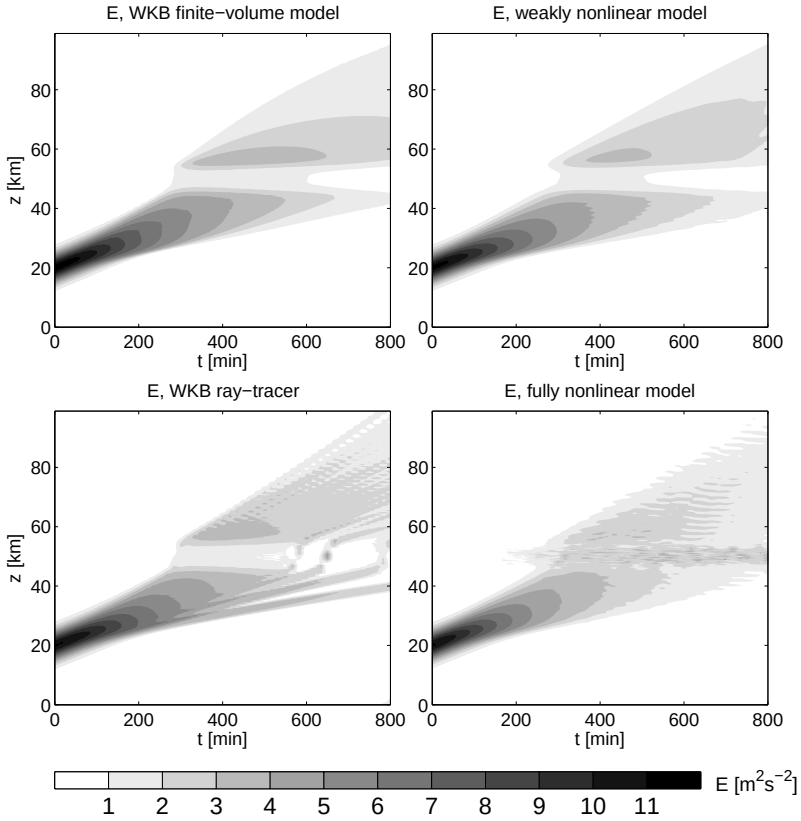

Figure 12. Horizontally averaged wave energy density of the wave packet propagating through a wind jet (for case 1).

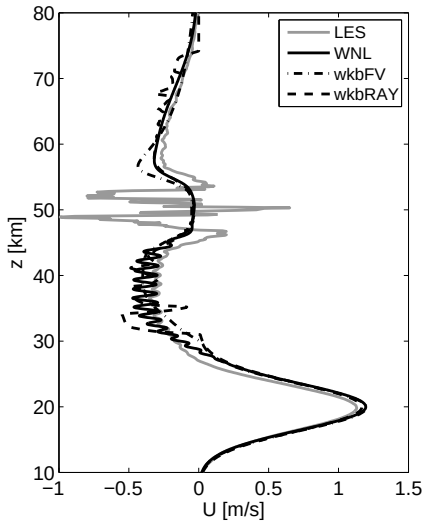

Figure 13. Wave-induced mean flow generated by the wave packet propagating through a wind jet (for case 1) at $t = 500$ minutes (LES: fully nonlinear wave-resolving model; WNL: weakly nonlinear wave-resolving model; wkbFV: Eulerian WKB finite-volume model; wkbRay: WKB ray tracer).

mean flow due to the waves was switched off (in the weakly nonlinear version, the solution in the wave-resolving models – but not in the WKB models – becomes very irregular below the reflecting level as the reflected waves propagate through the alternating induced mean flow, but this is unrelated to the caustics problem). Figure 18 shows the mean wave energy in the wave-resolving (linear) model and in the WKB models. The total wave energy in the layer just below the reflecting level reaches a plateau once the flux of downward- and upward-propagating waves become equal, and the value of the energy at the plateau is close to that calculated in the appendix for the steady-state case. As the width of the initial condition in wavenumber space is made smaller (the initial condition approaches a delta function), the analytic phase-space solution approaches the prediction of conventional physical-space ray-tracing, in which the wave-action density becomes infinite at the reflecting level but the wave-energy integrated over any interval (possibly including the reflecting level) converges to a constant finite value. The key property of the phase-space representation is that even as the group speed approaches zero, the wavenumber velocity remains nonzero, so points following the phase-space flow spend only a finite amount of time in the vicinity of the reflecting level.

6.5. *Modulationally unstable wave packets*

The final test case is a nonhydrostatic wave packet propagating through a uniformly stratified resting background. This is the test case used by Sutherland (2006b) to investigate modulational instability (see also Sutherland 2006a). A wave packet becomes modulationally unstable if its vertical wavelength is large enough compared to its horizontal wavelength (such that $|m| < 0.7|k|$). In this regime, the effect of the wave-induced mean flow is to decelerate the leading edge of the wave packet and accelerate the trailing edge, causing the packet to narrow and, if unstable, its amplitude to grow. The narrowing of the wave packet makes this test case inherently difficult for a model based on WKB theory, which assumes an amplitude envelope that varies

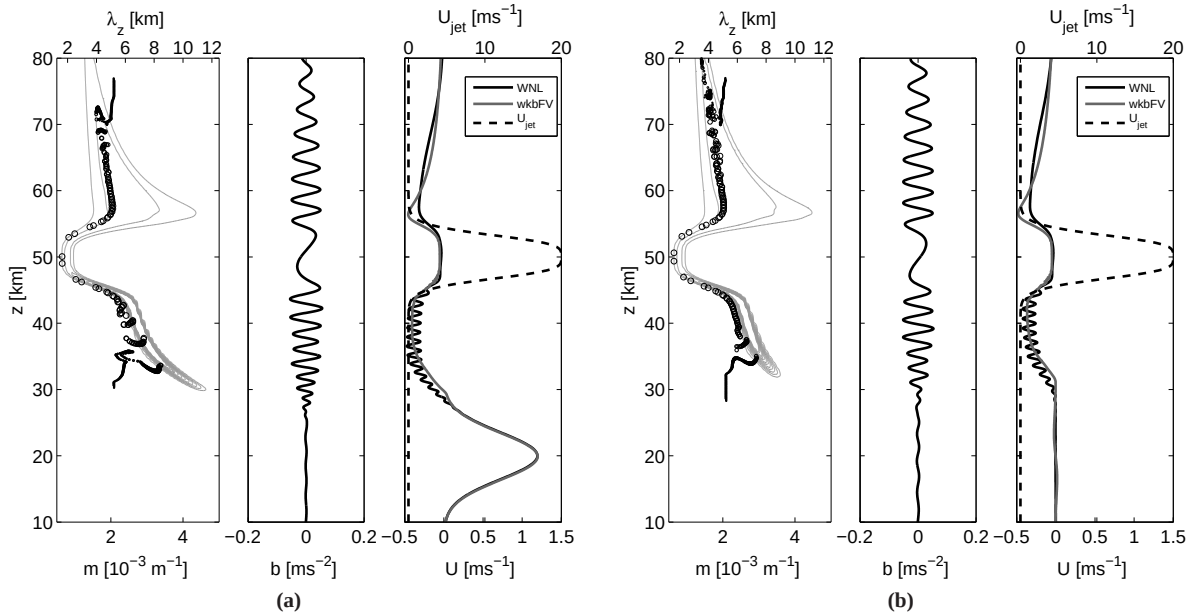

Figure 14. As in figure 7 but at $t = 500$ minutes in the test case with a wind jet. The dashed line in the right panels shows the wind jet $U_{jet}(z)$ (with values indicated on the upper horizontal axis). The contour interval for the wave-action density (left panels) is 5×10^5 m^3 s^{-1}.

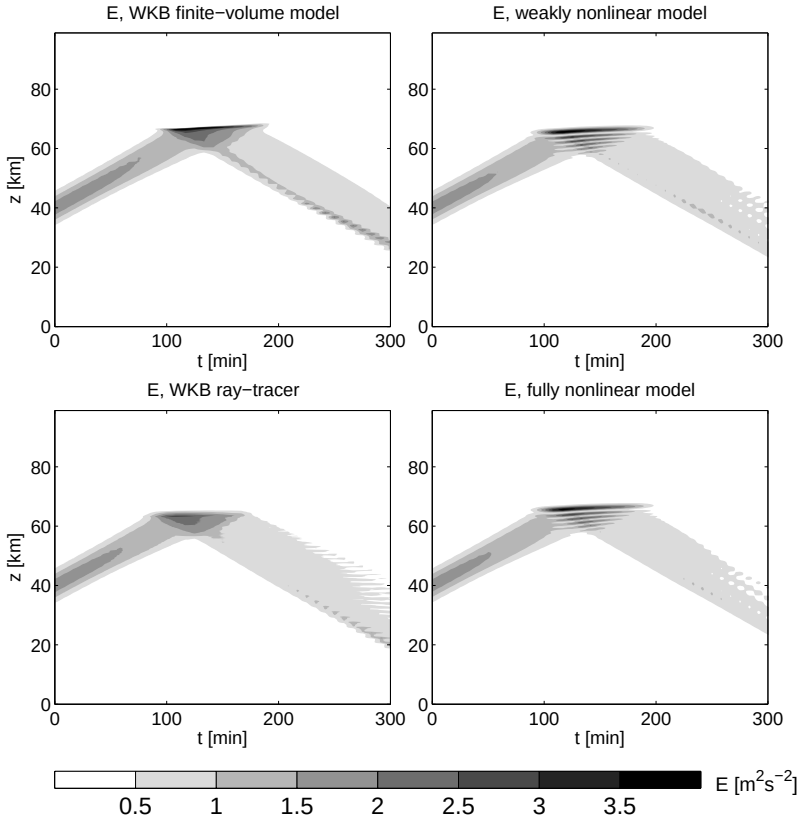

Figure 15. Horizontally averaged wave energy density of the wave packet reflected by a wind jet (for case 1).

slowly in space. Nevertheless, as will be shown, the WKB models remain well-behaved even in the most unstable case and reproduce some of the large-scale features of the solution if not the fine-scale details.

Three wave packets with horizontal wavelength $\lambda_x = 2$ km, half-width $\sigma = 3.2$ km and centres at $z_0 = 30$ km were simulated with the weakly nonlinear wave-resolving model and both WKB models in a vertical domain of height $l_z = 50$ km. The first case is a modulationally stable wave packet with initial vertical wavenumber $m_0 = -1.4k$ and amplitude $a_0 = 0.12$, the second is a "metastable" wave packet with $m_0 = -0.7k$ and $a_0 = 0.21$, and the third is a modulationally unstable wave packet with $m_0 = -0.4k$ and $a_0 = 0.42$. We present only the results from "case 2" – i.e. with the initial wave-induced mean flow (51) – but those from case 1 are similar. No LES simulations were done for

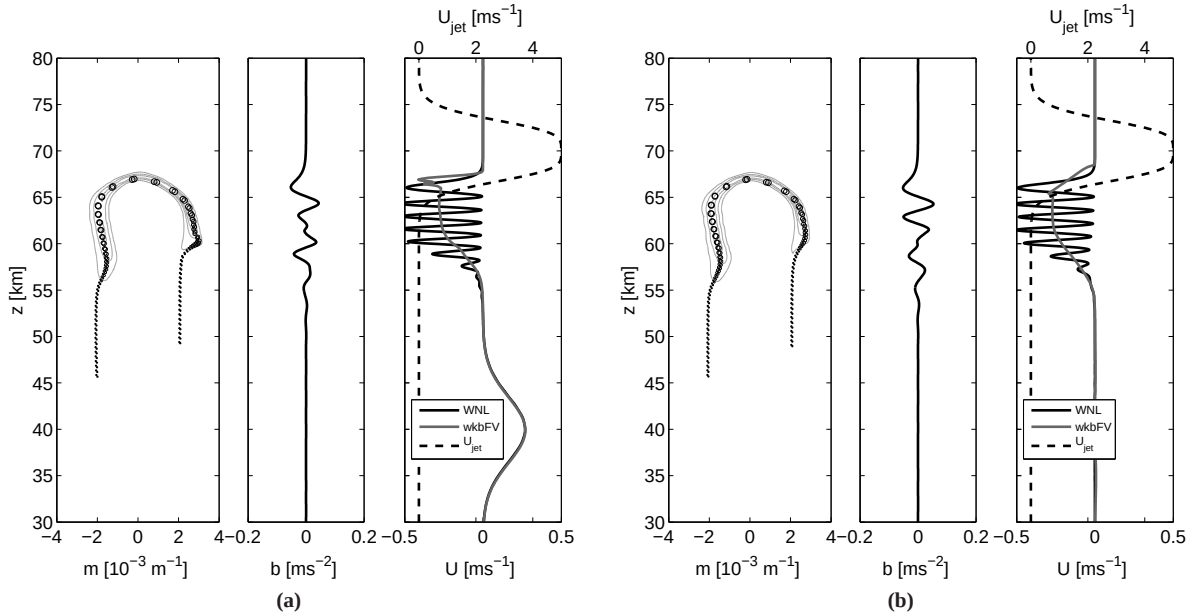

Figure 16. As in figure 14 but at $t = 140$ minutes in the test case with reflection by a wind jet. The contour interval for the wave-action density (left panels) is 5×10^4 m^3 s^{-1}.

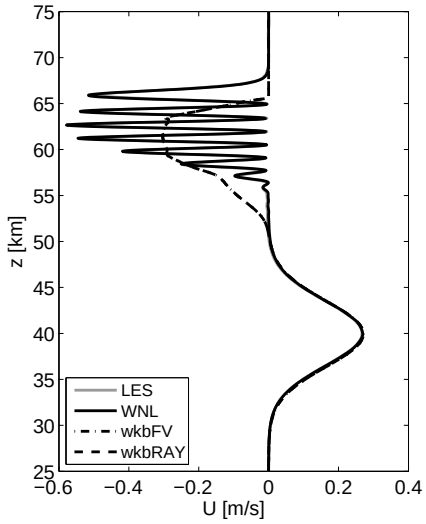

Figure 17. The wave-induced mean flow generated by the wave packet encountering a reflecting wind jet for case 1 at $t = 140$ minutes (LES: fully nonlinear wave-resolving model; WNL: weakly nonlinear wave-resolving model; wkbFV: Eulerian WKB finite-volume model; wkbRay: WKB ray tracer). Note that the agreement between the two WKB models and between the two validation models is so close that it is difficult to distinguish the two pairs of curves.

this experiment since the weakly nonlinear results closely match those of the fully nonlinear simulations reported in Sutherland's paper (his figure 3).

The spatial resolution for all models was twice as high as for the earlier test cases in order to accommodate the narrowing of the wave packet. The Eulerian WKB model used a wavenumber domain of -0.012 m$^{-1} < m < 0.002$ m^{-1} with $n_m = 1400$ cells in the m direction. As usual, the initial wave-action-density distribution had width in the wavenumber direction equivalent to one grid cell, or $\Delta m_0 = 10^{-4}$ m^{-1}. For the ray tracer, 400 ray particles were initialized in two columns between $z = 20$ km and $z = 40$ km on either side of $m = m_0$. Refer to table 2 for the full details.

Figure 19 shows the wave-induced mean flow simulated with all three models. To facilitate comparison with Sutherland (2006b), the mean flow is normalized by its maximum value in the initial condition and plotted in a reference frame moving with the initial group velocity of the wave packet.

The modulationally stable wavepacket (panel a) behaves similarly to the hydrostatic wavepacket in section 6.1 in that the wave-induced mean flow causes the wave packet to broaden. The WKB models agree well with the wave resolving model. On the other hand, the mean flow causes the metastable and unstable wave packets (panels b and c) to narrow and amplify and their centres to decelerate relative to their initial group speed. The WKB models capture this behaviour qualitatively quite well (although the Eulerian model overestimates the deceleration of the unstable wave packet). In the wave resolving simulations the mean flow develops a fine structure which is not captured by the WKB models. Although there are differences between the WKB and wave-resolving models, this is a case where a conventional ray-tracer would fail due to the formation of caustics (compare figure 1c, for which the mean flow induced by the metastable wave packet was used as the background for the rays).

7. Summary and discussion

WKB theory in position-wavenumber phase space has been used to develop a weakly nonlinear model for the evolution of internal gravity waves coupled to a time-dependent mean flow. Because standard WKB theory assumes that frequency and wavenumber are single-valued functions of time and space, it breaks down in the presence of caustics, such as those occurring in cases of wave reflection and in cases where a time-dependent background leads to wave packets overtaking each other. Contrary to

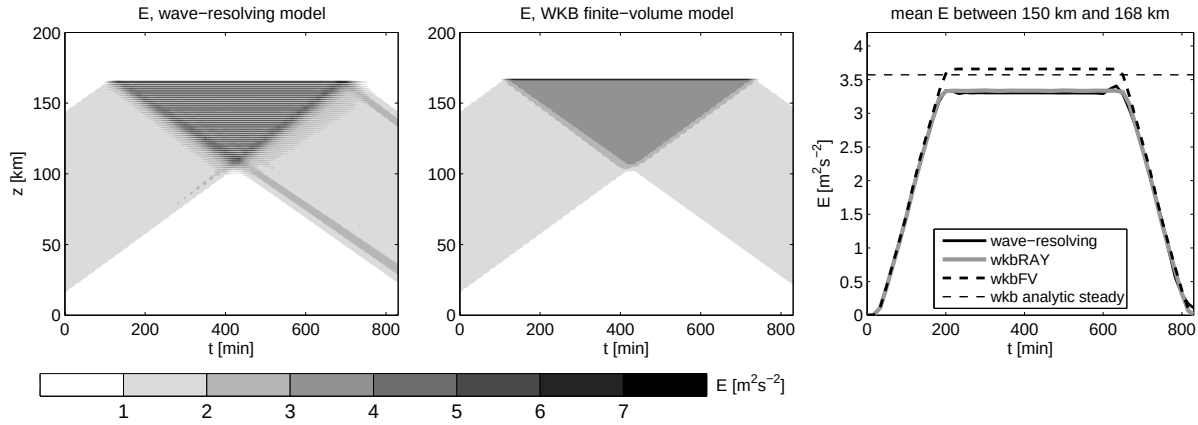

Figure 18. Horizontally averaged wave energy density of the very long wave packet reflected by a wind jet from the wave-resolving linear model and the WKB models (in linear mode). The right panel shows the mean energy in the layer between 150 and 168 km as a function of time. Once the downward (outgoing) waves balance the upward (incoming) waves, the wave energy reaches a plateau at the value corresonding to a case of a steady wave train reflected by a jet. The energy in the layer predicted by the analytic solution to the steady state WKB problem (see appendix B) indicated by dashed horizontal line.

practice in common gravity-wave-drag parameterizations, the interaction between small-scale gravity waves and solar tides (Senf and Achatz 2011) and between parameterized gravity waves and highly variable resolved gravity waves require that background transience be taken in account. Especially – but not only – under such circumstances, caustics can quickly become a problem. The caustics problem disappears in the phase-space approach used by Hertzog *et al.* (2002) and implemented here, where the ray equations for wavenumber and wave-action density in physical space (A) are replaced by a conservation equation for wave-action density in phase space $\mathcal{N}(m, z, t)$.

In passing from conventional WKB theory in physical space to WKB theory in phase space, one has some freedom to choose the exact form of the phase-space wave-action density function. The initial condition for $\mathcal{N}$ corresponding to the WKB ansatz for a quasimonochromatic wave packet has a delta-function dependence on wavenumber. In a numerical treatment of the phase-space WKB model, the delta function must be approximated by a wavenumber interval of nonzero phase-space wave-action density, the simplest example being uniform $\mathcal{N}$ in the interval between $m_0 - \frac{1}{2}\Delta m_0$ and $m_0 + \frac{1}{2}\Delta m_0$ and $\mathcal{N} = 0$ for all other m (equation 49). The size of Δm_0 is not related to and should not be confused with the width of the Fourier transform of the Gaussian envelope in physical space (i.e. inversely proportional to the width of the envelope). A convenient side-effect of a finite value of Δm_0 is that the phase-space wave-action density is nowhere infinite. Moreover, the *physical-space* wave-action density A (the integral of $\mathcal{N}$ over m) is also nowhere infinite, as it is in the conventional ray-tracing solution at the singular point in the example of a steady wave train being reflected by a shear layer (discussed in section 6.4 and appendix B). Because of the dependence of group velocity on wavenumber, the finite width of the initial condition also implies that the solution will spread out in space. As such, in extreme situations, such as near a reflecting level, the vertical distribution of energy density should be compared to a wave-resolving model or analytic solution in terms of averages over finite height intervals rather than in terms of point values. This is very compatible with a model using the finite-volume method which predicts averages over grid-cells rather than point values.

Two numerical implementations of the model have been shown to agree well with both a wave-resolving weakly nonlinear model and a fully nonlinear model. The Eulerian WKB model solves the phase-space wave-action-density conservation equation using a finite-volume method, and the Lagrangian WKB model transports ray particles with attached rectangular elements of constant area and wave-action density along rays in phase space. In both models, the mean flow evolves depending on the divergence of the momentum flux calculated by integrating a function of wave-action density either over the whole wavenumber dimension (Eulerian model) or over the area of each of the rectangular elements (Lagrangian model). The Lagrangian model is made more robust by allowing the rectangles attached to the ray particles to change shape depending on the straining effect of the phase space flow. This extra degree of flexibility allows the model to give good results with fewer ray particles (a comparable result can be obtained in many cases with rectangles of fixed shape and more ray particles per unit length in the vertical).

For problems like the propagation of a single wave packet, where the wave-action-density distribution is highly localized in position and wavenumber, the Eulerian model is inefficient because it must integrate the wave-action-density equation over a domain large enough to include all positions and wavenumbers accessible to the wave packet. Due to the conservation of wave-action density along phase-space rays, the Lagrangian model only needs to integrate the ray equations on a set of ray particles that initially covers the region of nonzero $\mathcal{N}$. Also, for a more realistic case of waves propagating in an environment varying in all three dimensions, the Eulerian approach would require a six-dimensional computational domain and is thus less practical with present computational capabilities. On the other hand, the Eulerian model uses a very robust numerical scheme, does not require smoothing of the momentum flux, and generally agrees better with the weakly nonlinear wave-resolving model (see figures 10, 11 and 12). Furthermore, in the case of an initially broad spectrum of waves, the Eulerian model can be competitive with the Lagrangian in terms of performance. Eulerian wave-action models are in operational use for oceanic surface-wave forecasting (where

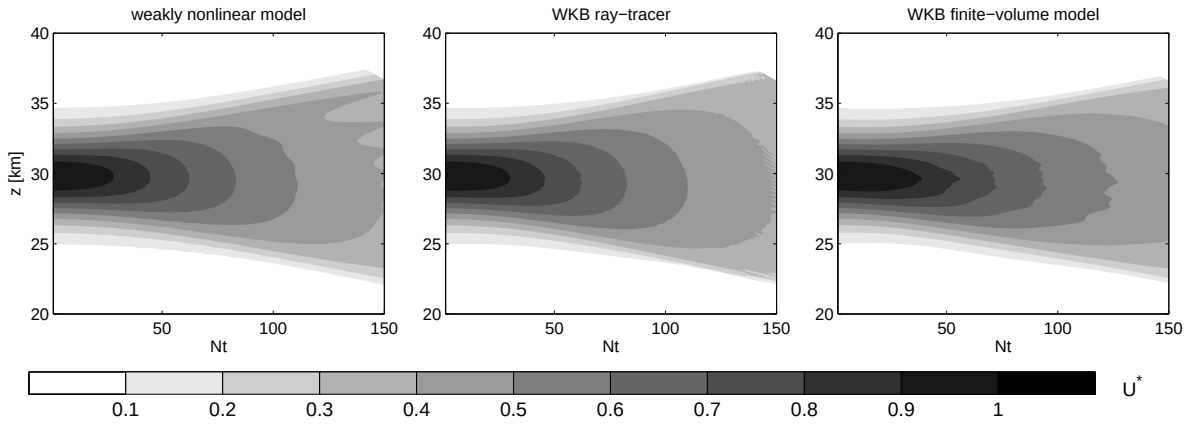

(a)

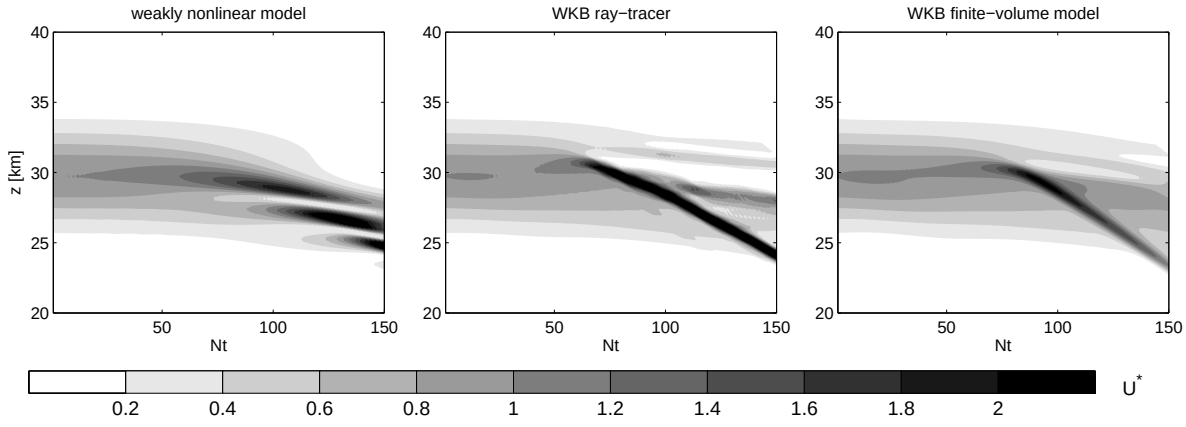

(b)

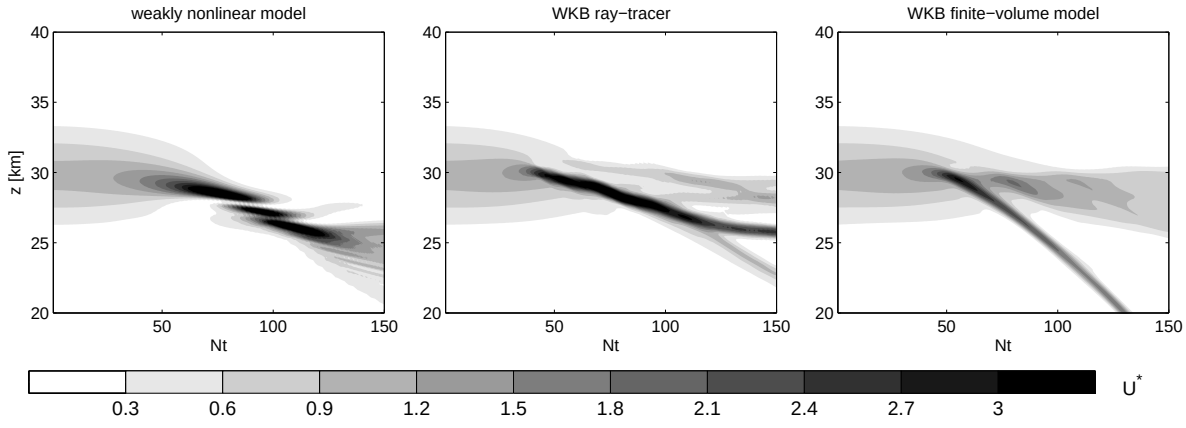

(c)

Figure 19. Normalized wave-induced mean flow from the modulational instability experiment simulated with the weakly nonlinear wave-resolving model and both WKB models: (a) stable case ($m_0 = -1.4k$, $a_0 = 0.12$), (b) metastable case ($m_0 = -0.7k$, $a_0 = 0.21$), and (c) unstable case ($m_0 = -0.4k$, $a_0 = 0.42$). Plots are in the reference frame moving with the initial group speed at the centre of the wave packet.

either a four-dimensional position-wavenumber or a four-dimensional position-frequency-direction phase space is needed), so clearly a two-dimensional atmospheric gravity-wave problem can also be solved operationally. Since the heaviest computational effort in oceanic wave-action models relates to the computation of the *nonlinear* four-wave-interaction component, there is hope that the approach could also be suitable for solving the merely *weakly* nonlinear problem of three-dimensional gravity waves in the atmosphere without extensive further simplification.

Five test cases were presented: (i) a nearly hydrostatic gravity wave packet propagating upward through an initially resting background with uniform stratification; (ii) the same wave packet propagating through a background stratification varying slowly with height (but not with time); (iii) the same wave packet propagating through and being

refracted by a localized wind jet; (iv) a nonhydrostatic wave packet being reflected by a sufficiently intense wind jet; (v) a nonhydrostatic wave packet subject to modulational instability when its vertical wavelength becomes large enough compared to its horizontal wavelength. In each case caustics occur, either due to the waves encountering a reflecting jet, or due to transience in the background associated with feedback of the waves on the background. All experiments were done with and without an initial mean flow perturbation that propagates together with the wave packet. Other than near the height where the wave packet is initialized, there are only small differences between the results with and without the extra initial mean flow.

In all cases the WKB models agree well with the wave-resolving models, with the partial exception of the most modulationally unstable nonhydrostatic wave packet. The latter was always going to be a challenge for the WKB models since the amplitude variation is on the same scale as the vertical wavelength. Otherwise, the most prominent difference is the formation of small-scale structures in the induced horizontal mean flow in the wave-resolving models in cases where the wave packet propagates through a nonuniform background. These structures probably arise through wave-wave interactions which the WKB models cannot account for. In most cases they have a weak effect on the large scale structures and on the propagation of the waves (but they might have other consequences for local mixing and turbulence and would be worthy of study in their own right). In all cases the weakly nonlinear and the fully nonlinear models produce similar results, indicating that higher harmonics of the waves do not play a significant role in the propagation of vertically compact horizontally periodic wave packets. It is sufficient to represent the wave-induced mean flow (as observed by Sutherland 2006b). The only significant difference between the two wave-resolving models occurs in the case where the wave packet is refracted by a background wind jet. The fully nonlinear model is the only one to develop small-scale structures in the wave-induced mean flow within the region of the background jet.

While we have focused exclusively on a one-dimensional wave packet with a horizontal mean background flow, the phase-space WKB theory with mean-flow coupling generalizes to any number of spatial dimensions. While the Eulerian model as implemented here could quickly become computationally intractable in more than one dimension, the Lagrangian approach seems promising for application in an improved parameterization of unresolved gravity waves in a weather or climate model. Most current schemes neglect both the horizontal propagation of wave packets and the effect of horizontal variations on their propagation, even though these have been shown to be important (Song and Chun 2008; Hasha *et al.* 2008; Senf and Achatz 2011).

For applying the phase-space WKB models to the gravity-wave-drag parameterization problem, the Boussinesq approximation would have to be relaxed so that the amplitude of the waves can grow as the ambient density decreases. For that reason, adapting both WKB models to the pseudo-incompressible equations (Durran 1989), is the subject of ongoing work. In addition, a rule would be needed for depositing momentum to the mean flow when the waves reach overturning (breaking) amplitude, such as maintaining the wave-action density at the threshold for static stability above the breaking height, resulting in an enhanced forcing of the mean flow (along the lines of Lindzen 1981). Similar considerations might be necessary with regard to other nonlinear dissipation mechanisms such as modulational instability.

A. Static stability of a wave packet in a varying background

A flow of a Boussinesq fluid (governed by equations 1) is statically stable if the local vertical buoyancy gradient is everywhere less than the mean squared background buoyancy frequency N^2. During the passage of an internal-gravity-wave packet with buoyancy amplitude $\hat{b} = aN^2/m$, the flow is everywhere stable if the nondimensional amplitude of the waves satisfies $|a| < 1$. In this section we examine the purely linear variation of a as an initially stable wave packet propagates through a background stratification varying with height.

Suppose the centre of the wave packet is initially located at height z_0 and the waves have vertical wavenumber m_0 and amplitude a_0 at time t_0. Suppose further that the background stratification varies with height, with $N(z_0) = N_0$. One might expect that the system is most likely to become statically unstable when the waves reach the height where the background is *least* statically stable, and thus that static instability is possible only if $|a_0| > \min(N^2/N_0^2)$. In fact, however, one can show from WKB theory that the wavelength and amplitude of the waves change as the background changes such that static instability is most likely where the background is *most* stable.

For simplicity assume the background wind is zero (thereby neglecting the momentum flux due to the waves) and the background stratification is independent of time. From (20c), the wave frequency ω is therefore conserved following the group velocity, and from the dispersion relation (11) one has

$$m^2(z_c) = \frac{N^2(z_c)}{N_0^2}(k^2 + m_0^2) - k^2 \,, \tag{59}$$

where $z_c(t)$ is the height of the centre of the wave packet at time t.

Since the centre of the wave packet moves with the local group velocity, the wave-action density at the centre of the wave packet A_c obeys

$$\frac{\mathrm{d}A_c}{\mathrm{d}t} = \frac{\mathrm{d}A_c}{\mathrm{d}z_c}\frac{\mathrm{d}z_c}{\mathrm{d}t} = c_{gz}(z_c)\frac{\mathrm{d}A_c}{\mathrm{d}z_c} = -A_c\frac{\mathrm{d}c_{gz}}{\mathrm{d}z_c} \,, \tag{60}$$

where the ray equation for wave action (20d) has been used. Equation (60) implies that $c_{gz}(z_c)A_c$ is constant. Using (14), (20a), and the assumption that ω is constant following the centre of the wave packet, (60) and (59) give

$$|a(z_c)|^2 = \frac{m(z_c)}{m_0}|a_0|^2 \tag{61}$$

$$= |a_0|^2\left[\frac{N^2(z_c)}{N_0^2}\left(\frac{k^2}{m_0^2}+1\right) - \frac{k^2}{m_0^2}\right]^{\frac{1}{2}} \,. \tag{62}$$

Therefore, if $|a_0| < 1$, then $|a(z_c)|$ can only exceed unity where

$$\frac{N^2(z)}{N_0^2} > \frac{|a_0|^{-4} + \frac{k^2}{m_0^2}}{1 + \frac{k^2}{m_0^2}} > 1 \,, \tag{63}$$

that is, where the background static stability is *increased* relative to N_0.

If the perturbation to the background stratification takes the form of a large-scale gravity wave with nondimensional amplitude a_{back}, then $\max(N^2) = N_0^2(1 + |a_{back}|)$. Static instability will only occur if

$$|a_{back}| > \frac{|a_0|^{-4} - 1}{1 + (k/m_0)^2} \,. \tag{64}$$

For the hydrostatic waves used in the experiment with variable stratification in section 6.2, as $|a_{back}| \to 1$, the initial wave packet amplitude $|a_0|$ would have to be at least 0.76 for the possibility of static instability occurring. In a more general case with feedback from the waves on the large scale flow, the interaction of a statically stable hydrostatic wave packet with a statically stable large scale wave is unlikely to ever lead to static instability.

B. Energy density in a steady linear wave train reflected by a shear flow

An analytic solution may be derived for the energy density as a function of height for the steady-state linear version (i.e., without feedback of the waves onto the mean flow) of the test case, described in section 6.4, featuring waves reflected by a jet.

Suppose that at the height z_0 the phase-space wave-action density is uniformly distributed between the positive wavenumbers m_{10} and m_{20} with value $\mathcal{N}_0$ and zero for all other positive m, cf. (49). In a steady-state solution, the region of nonzero wave-action density is confined between the two characteristic curves $m_1(z)$ and $m_2(z)$ passing through the points $m_1(z_0) = m_{10}$ and $m_2(z_0) = m_{20}$. Since the background is independent of time, the characteristics are curves of constant Ω_-, such that for the curve $m_j(z)$,

$$\Omega_-[z, m_j(z)] = kU(z) - \frac{kN}{\sqrt{k^2 + m_j^2(z)}} \equiv \omega_j \tag{65}$$

is constant (by symmetry we need consider only the upward propagating branch, with $k > 0$, $m > 0$ and $\hat{\omega} < 0$). This may be rearranged to yield

$$m_j^2(z) = \frac{N^2}{\hat{c}_{pj}^2(z)} - k^2, \tag{66}$$

where $\hat{c}_{pj}(z) = \omega_j/k - U(z)$ is the intrinsic horizontal phase speed. The reflecting level z_j^r is the minimum z for which $m_j(z) = 0$, i.e. such that

$$\hat{c}_{pj}(z_j^r) = -\frac{N}{k}. \tag{67}$$

The energy density as a function of z is, by the definition (52),

$$E(z) = 2\mathcal{N}_0 \begin{cases} \displaystyle\int_{m_1(z)}^{m_2(z)} \hat{\omega}(m)\mathrm{d}m, & z < z_1^r \\ \displaystyle\int_{0}^{m_2(z)} \hat{\omega}(m)\mathrm{d}m, & z_1^r < z < z_2^r \\ 0 & z > z_2^r \end{cases} \tag{68}$$

where the factor 2 accounts for the upward and downward propagating branches.

The integral of the intrinsic frequency is, for constant N and k,

$$\begin{aligned} \int \hat{\omega}(m)\mathrm{d}m &= N \int \frac{1}{\sqrt{1 + \frac{m^2}{k^2}}} \mathrm{d}m \\ &= Nk \log \left| \frac{m}{k} + \sqrt{1 + \frac{m^2}{k^2}} \right| \\ &\qquad + \text{a constant}, \end{aligned} \tag{69}$$

so that

$$\begin{aligned} E(z) = 2Nk\mathcal{N}_0 \\ \times \begin{cases} \log \left| \frac{m_2(z)}{k} + \sqrt{1 + \frac{m_2^2(z)}{k^2}} \right| & \\ \quad - \log \left| \frac{m_1(z)}{k} + \sqrt{1 + \frac{m_1^2(z)}{k^2}} \right| & , \; z < z_1^r \\ \log \left| \frac{m_2(z)}{k} + \sqrt{1 + \frac{m_2^2(z)}{k^2}} \right| & , \; z_1^r < z < z_2^r \\ 0 & , \; z > z_2^r \end{cases} \end{aligned} \tag{70}$$

Figure 20 shows, for various values of $\Delta m_{00} \equiv m_{20} - m_{10}$ (indicated by different shades of grey), the phase-space region of nonzero $\mathcal{N}$ and the energy density as a function of height for a steady train of waves with horizontal and average vertical wavelength (far from the reflecting level) 3 km and amplitude $a_0 = 0.2$ at $z = z_0$ encountering the background jet (56) used in the test case. As Δm_{00} becomes small, the graph approaches that of the prediction of conventional ray-tracing (in physical space)

$$\frac{E_{conv}(z)}{E(z_0)} = \frac{m_{00}}{m_0(z)} \left[\frac{k^2 + m_0^2(z)}{k^2 + m_{00}^2} \right] , \tag{71}$$

where $m_{00} = \frac{1}{2}(m_{10} + m_{20})$, indicated by the heavy dashed line. The latter becomes infinite at the singular reflecting level, while the solution (70) remains finite for all finite Δm_{00}. The equivalence of (70) and (71) in the limit $\Delta m_{00} \to 0$ can be shown analytically by expanding the integrand in (68) in a Taylor series in $m(z) - m_1(z)$, integrating, and then using (66) to calculate the leading order dependence of $m_2(z) - m_1(z)$ on Δm_{00}. For comparison the energy density versus height from the linear simulation with the finite-volume phase-space WKB model is also shown in figure 20. It is smoother than the analytic result due to the diffusion inherent to the numerical method. The mean energy density in the layer 150 km $< z <$ 168 km converges to a constant as $\Delta m_{00} \to 0$ and is close to the value observed in the wave-resolving and WKB models (compare right panels of figures 20 and 18).

Acknowledgements

U.A. and S.H. thank Deutsche Forschungsgemeinschaft for partial support through the MetStröm (Multiple Scales in Fluid Mechanics and Meteorology) Priority Research Program (SPP 1276), and through Grants HI 1273/1-2 and Ac71/4-2. The authors thank Fabian Senf for helpful comments on an earlier version of the manuscript.

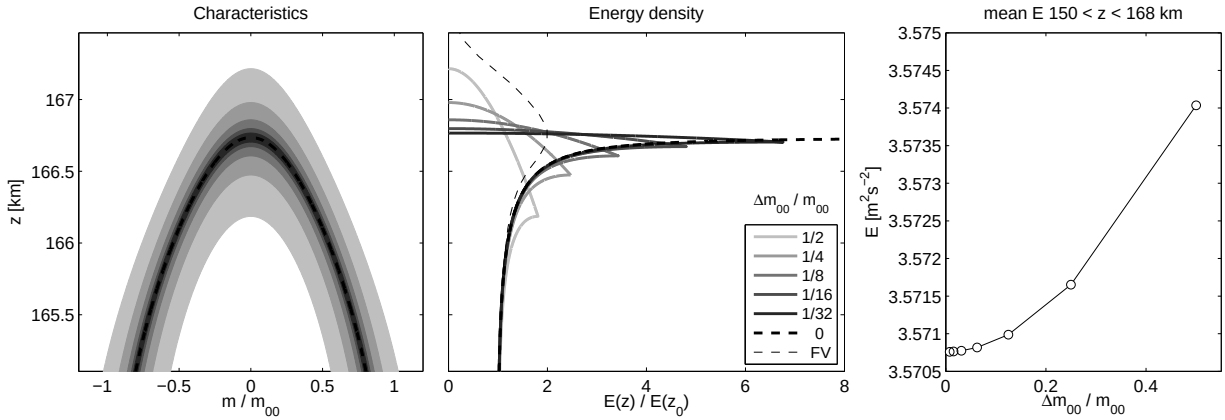

Figure 20. Phase-space region of nonzero $\mathcal{N}$ bounded by characteristics $m_1(z)$ and $m_2(z)$ (left) and energy density versus height (middle) for a steady wave train encountering the jet (56), plotted for different values of $\Delta m_0/m_0$. The prediction of conventional ray tracing (in physical space) is indicated by the heavy dashed line ("$\Delta m_{00} = 0$"), and the energy density from the finite-volume model is indicated by the fine dashed line ("FV"). Right panel: average energy density in the interval 150 km $< z <$ 168 km (compare with right panel of figure 18).

References

Achatz U, Klein R, Senf F. 2010. Gravity waves, scale asymptotics and the pseudo-incompressible equations. *J. Fluid Mech.* **663**: 120–147.

Acheson DJ. 1976. On over-reflexion. *J. Fluid Mech.* **77**: 433–472.

Alexander MJ, Dunkerton TJ. 1999. A spectral parameterization of mean-flow forcing due to breaking gravity waves. *J. Atmos. Sci.* **56**: 4167–4182.

Alexander MJ, Geller M, McLandress C, Polavarapu S, Preusse P, Sassi F, Sato K, Eckermann SD, Ern M, Hertzog A, Kawatani Y, Pulido M, Shaw TA, Sigmond M, Vincent R, Watanabe S. 2010. Recent developments in gravity-wave effects in climate models and the global distribution of gravity-wave momentum flux from observations and models. *Quart. J. R. Met. Soc.* **136**(650): 1103–1124.

Benoit M, Marcos F, Becq F. 1996. Development of a third generation shallow-water wave model with unstructured spatial meshing. In: *Proceedings of 25th International Conference on Coastal Engineering*. Am. Soc. of Civ. Eng.: New York, pp. 465–478.

Booij N, Ris R, Holthuijsen L. 1999. A third-generation wave model for coastal regions. I – Model description and validation. *J. Geophys. Res.* **104**(C4): 7649–7666.

Bretherton F. 1966. The propagation of groups of internal gravity waves in a shear flow. *Quart. J. Roy. Met. Soc.* **92**: 466–480.

Bretherton F, Garrett C. 1968. Wavetrains in inhomogeneous moving media. *Proc. Roy. Soc. Lond. A* **302**: 529–554.

Broutman D, Ma J, Eckermann SD, Lindeman J. 2006. Fourier-ray modeling of transient trapped lee waves. *Mon. Wea. Rev.* **134**: 2849–2856.

Broutman D, Rottman J. 2002. Maslov's method for stationary hydrostatic mountain waves. *Quart. J. Roy. Meteor. Soc.* **128**: 1159–1172.

Broutman D, Rottman J, Eckermann SD. 2004. Ray methods for internal waves in the atmosphere and ocean. *Annu. Rev. Fluid Mech.* **36**: 233–253.

Broutman D, Young WR. 1986. Interaction of small-scale oceanic internal waves with near-inertial waves. *J. Fluid Mech.* **166**: 341–358.

Brown MG. 2000. The Maslov integral representation of slowly varying dispersive wavetrains in inhomogeneous moving media. *Wave Motion* **32**: 247–266.

Bühler O. 2009. *Waves and Mean Flows*. Cambridge University Press.

Bühler O, McIntyre ME. 1999. On shear-generated gravity waves that reach the mesosphere. Part II: Wave propagation. *J. Atmos. Sci.* **56**: 3764 –3773.

Dewar R. 1970. Interaction between hydromagnetic waves and a time-dependent, inhomogeneous medium. *Phys. Fluids* **13**: 2710–2720.

Dietrich J, Zijlema M, Westerink J, Holthuijsen L, Dawson C, Luettich Jr R, Jensen R, Smith J, Stelling G, Stone G. 2011. Modeling hurricane waves and storm surge using integrally-coupled, scalable computations. *Coast. Eng.* **58**(1): 45–65.

Dosser HV, Sutherland BR. 2011. Anelastic internal wave packet evolution and stability. *J. Atmos. Sci.* **68**: 2844–2859.

Dubrulle B, Nazarenko S. 1997. Interaction of turbulence and large-scale vortices in incompressible 2D fluids. *Physica D* **110**: 123–138.

Durran DR. 1989. Improving the anelastic approximation. *J. Atmos. Sci.* **46**: 1453–1461.

Durran DR. 2010. *Numerical Methods for Fluid Dynamics*. Springer.

Eckermann SD. 1992. Ray-tracing simulation of the global propagation of inertia gravity waves through the zonally averaged middle atmosphere. *J. Geophys. Res.* **97**: 15,849–15,866.

Fritts DC, Alexander MJ. 2003. Gravity wave dynamics and effects in the middle atmosphere. *Rev. Geophys.* **41**: 1003.

Fritts DC, Dunkerton TJ. 1984. A quasi-linear study of gravity-wave saturation and self-acceleration. *J. Atmos. Sci.* **41**: 3272–3289.

Grimshaw R. 1975. Internal gravity waves: critical layer absorption in a rotating fluid. *J. Fluid Mech.* **70**: 287–304.

Hasha A, Bühler O, Scinocca JF. 2008. Gravity wave refraction by three-dimensionally varying winds and the global transport of angular momentum. *J. Atmos. Sci.* **65**: 2892–2906.

Hayes W. 1970. Kinematic wave theory. *Proc. Roy. Soc. Land. A* **320**: 209–226.

Hertzog A, Souprayen C, Hauchecorne A. 2002. Eikonal simulations for the formation and the maintenance of atmospheric gravity wave spectra. *J. Geophys. Res.* **107**: D12:4145.

Hickel S, Adams N, Domaradzki A. 2006. An adaptive local deconvolution method for implicit LES. *J. Comput. Phys.* **213**: 413–436.

Kemm F. 2010. A comparative study of TVD-limiters: Well-known limiters and an introduction of new ones. *Int. J. Numer. Meth. Fluids* **67**: 404–440.

Kim YJ, Eckermann SD, Chun HY. 2003. An overview of the past, present and future of gravity-wave drag parameterization for numerical climate and weather prediction models. *Atmosphere-Ocean* **41**(1): 65–98.

Lighthill J. 1978. *Waves in Fluids*. Cambridge University Press.

Lindzen RS. 1981. Turbulence and stress owing to gravity wave and tidal breakdown. *J. Geophys. Res.* **86**(C10): 9707–9714.

Marks CJ, Eckermann SD. 1995. A three-dimensional nonhydrostatic ray-tracing model for gravity waves: Formulation and preliminary results for the middle atmosphere. *J. Atmos. Sci.* **52**: 1959–1984.

Müller P. 1976. On the diffusion of momentum and mass by internal gravity waves. *J. Fluid Mech.* **77**: 789–823.

Remmler S, Hickel S. 2012. Direct and large eddy simulation of stratified turbulence. *Int. J. Heat Fluid Flow* **35**: 13–24.

Remmler S, Hickel S. 2013. Spectral structure of stratified turbulence: direct numerical simulations and predictions by large eddy simulation. *Theor. Comp. Fluid Dyn.* **27**(3-4): 319–336.

Roland A, Cucco A, Ferrarin C, Hsu TW, Liau JM, Ou SH, Umgiesser G, Zanke U. 2009. On the development and verification of a 2-D

coupled wave-current model on unstructured meshes. *J. Marine Syst.* **78**: S244–S254.

Roland A, Zhang YJ, Wang HV, Meng Y, Teng YC, Maderich V, Brovchenko I, Dutour-Sikiric M, Zanke U. 2012. A fully coupled 3D wave-current interaction model on unstructured grids. *J. Geophys. Res.* **117**: C00J33:1–18.

Scinocca JF, Shepherd TG. 1992. Nonlinear wave-activity conservation laws and Hamiltonian structure for the two-dimensional anelastic equations. *J. Atmos. Sci.* **49**: 5–27.

Senf F, Achatz U. 2011. On the impact of middle-atmosphere thermal tides on the propagation and dissipation of gravity waves. *J. Geophys. Res.* **116**: D24 110.

Song IS, Chun HY. 2008. A Lagrangian spectral parameterization of gravity wave drag induced by cumulus convection. *J. Atmos. Sci.* **65**: 1204–1224.

Sutherland BR. 2001. Finite-amplitude internal wavepacket dispersion and breaking. *J. Fluid Mech.* **429**: 343–380.

Sutherland BR. 2006a. Internal wave instability: Wave-wave versus wave-induced mean flow interactions. *Phys. Fluids* **18**: 074 107.

Sutherland BR. 2006b. Weakly nonlinear internal gravity wavepackets. *J. Fluid Mech.* **569**: 249–258.

Sutherland BR. 2010. *Internal Gravity Waves*. Cambridge University Press.

Tolman HL. 1991. A third-generation model for wind waves on slowly varying, unsteady and inhomogeneous depths and currents. *J. Phys. Oceanogr.* **21**: 782–797.

Vanderhoff JC, Nomura KK, Rottman JW, Macaskill C. 2008. Doppler spreading of internal gravity waves by an inertia-wave packet. *J. Geophys. Res.* **113**: C05 018.

Vanderhoff JC, Rottman JW, Broutman D. 2010. The trapping and detrapping of short internal waves by an inertia wave. *Phys. Fluids* **22**: 126 603.

WAMDI Group. 1988. The WAM model – a third generation ocean wave prediction model. *J. Phys. Oceanogr.* **18**: 1775–1810.

Warner CD, McIntyre ME. 2001. An ultrasimple spectral parameterization for nonorographic gravity waves. *J. Atmos. Sci.* **58**: 1837–1857.

Watanabe S, Kawatani Y, Tomikawa Y, Miyazaki K, Takahashi M, Sato K. 2008. General aspects of a T213L256 middle atmosphere general circulation model. *J. Geophys. Res.* **113**: D2110:1–23.